Convective mass-flux from long term radar reflectivities over Darwin, Australia

Alessandro C. M. Savazzi[1], Christian Jakob[2,3], A. Pier Siebesma[1,4]

[1]Department of Geoscience and Remote Sensing, Delft University of Technology, Delft, the Netherlands
[2]School of Earth, Atmosphere and Environment, Monash University, Melbourne, Victoria, Australia
[3]ARC Centre of Excellence for Climate Extremes, Monash University, Melbourne, Victoria, Australia
[4]Royal Netherlands Meteorological Institute (KNMI), De Bilt, the Netherlands

Key Points:

- An observationally based data set of convective mass-flux spanning more than a decade is developed and analysed.
- The data set provides for the first time long-term observational estimates of net entrainment.
- There is strong bulk entrainment in the lowest 4 km of the atmosphere and strong detrainment above that level.

Corresponding author: Alessandro Savazzi, A.C.M.Savazzi@tudelft.nl

Abstract

Most cumulus parametrizations today make use of a simple conceptual model of convection, called the mass-flux approach. This approach depicts convection as an ensemble of updrafts and downdrafts occurring within a model grid-box. The aim of this study is to determine convective mass-fluxes and their constituents on the scale of a 100 km GCM grid-box from a C-band polarimetric radar and thereafter investigate the relative role of area fraction and vertical velocity in determining the shape and magnitude of bulk mass-flux profiles. We make use of observational estimates of these quantities spanning 13 wet seasons in the tropical region of Darwin. Following a bulk approach, the results show that the distribution of mass-flux is positively skewed and its mean profile peaks at 4 km. This is the result of constant area fractions and increasing vertical velocities below that level. Above 4 km, in-cloud vertical velocity plays a marginal role compared to the convective area fraction in controlling mass-flux profiles.

1 Introduction

It has long been recognised that deep convective systems play a key role in regulating the large scale circulations and thermal structure of the atmosphere in the tropics (Riehl & Malkus, 1958, 1979; Emanuel et al., 1994; Simpson et al., 1998; de Rooy et al., 2008; Labbouz et al., 2018). Despite this, the underlying physical processes connected to convective clouds and their response to a warmer climate are not yet fully understood.

Cumulus convection is observed to organise into strong narrow updrafts which cover a small horizontal fraction of the large-scale atmosphere (e.g., Oerlemans, 1986; Davies et al., 2013; Louf et al., 2019). Because of the limited spatial resolution of General Circulation Models (GCMs), atmospheric convection occurs at a sub-grid scale and, thus, must be parameterized (Arakawa, 2004). As a result, progress in simulating clouds and precipitation in GCMs strongly relates to improvements in the cumulus cloud parameterizations and their coupling to boundary layer and cloud processes (e.g., Bechtold et al., 2008; Jakob, 2010).

Most cumulus parametrizations today make use of a simple conceptual model of convection, called the mass-flux approach (e.g., Ooyama, 1971; Yanai et al., 1973; Arakawa et al., 1974; Tiedtke, 1989). This approach depicts convection as an ensemble of updrafts and downdrafts occurring within a model grid-box. The area covered by the up- and downdrafts is assumed to be small compared to the grid-size. The mass-flux for an individual draft is defined as the product of the air density, the fractional area covered by the draft and the vertical velocity inside it. Most commonly, parametrizations apply the so-called bulk-mass-flux approach (e.g., Tiedtke, 1989; Gregory & Rowntree, 1990), where only the average properties of the cloud ensemble are considered. The alternative spectral approach, where different cloud types are assumed to co-exist or even compete with each other (e.g., Arakawa et al., 1974; Wagner & Graf, 2010) , while available, is less commonly used due to computational constraints. The essential assumption in either approach is that the vertical transport of any scalar is well represented by the product of the mass-flux and the bulk updraft scalar excess with respect to the updraft environment.

While conceptually simple, the evaluation of mass-flux approaches is challenging as it requires concurrent knowledge of the fractional area covered by convective clouds and the vertical velocity inside the clouds in domain of roughly 100 km at a side to match current global climate model resolutions. As a result, much of the evaluation and parameter estimation for mass-flux schemes has relied on the use Cloud-Resolving and Large-Eddy Simulation Models (e.g., A. P. Siebesma et al., 1996; de Rooy et al., 2008; A. Siebesma et al., 2020). These model experiments are often limited to short temporal extent and idealised atmospheric conditions. Furthermore, they show limits in reproducing convective organisation and taking into account the large scale conditions (Schalkwijk et al., 2015; Schemann et al., 2020).

The few observational estimates of mass-fluxes that exist for deep convection, are based on short-term field campaigns. Early on, heat and water budget analyses applied to radiosonde-arrays were combined with some simple assumptions to provide indirect estimates of the bulk-properties of convective mass-fluxes in both deep (e.g., Yanai et al., 1973) and shallow convection (e.g., Nitta & Esbensen, 1974; Nitta, 1975). Direct measurements of vertical velocities in convection became available from aircraft campaigns (e.g., Byers & Braham, 1949; Marwitz, 1973; LeMone & Zipser, 1980; Anderson et al., 2005; May et al., 2008). While providing several breakthroughs in our understanding of tropical convection, the small-scale nature of these observations and the absence of concurrent knowledge of the distribution of clouds over a large area prevents their use in evaluating the mass-flux concept.

More recently, long-time radar observations from both space and the ground have been used to extensively study the behaviour of tropical convection and its relationship to state of the larger-scale atmosphere. Examples include the Tropical Rainfall Measurement Mission (TRMM, (Kummerow et al., 1998)) data sets to study convective characteristics, such as convective vigour (Zipser, 2003), types of convective systems (Nesbitt et al., 2000; Jr. et al., 2015) and the role of stratiform processes in tropical rainfall (Schumacher & Houze, 2003). Recent studies using a more than a decade long calibrated radar data set acquired at Darwin, Australia, (Jackson et al., 2018) specifically retrieved the fractional area covered by convection and related it to precipitation and the large-scale sate of the atmosphere (e.g., Davies et al., 2013; Louf et al., 2019). They found that convective rainfall in the radar domain ($\approx$130 km radius) was very strongly related to the area fraction of active convective cells and that this area fraction was generally small. This important finding indicated that predicting area fraction is an important step in determining precipitation and hence the overall heating in a convecting column.

Long-term measures of vertical velocity are not as trivial to obtain as for area fraction. Nevertheless, they are essential for a better evaluation of the mass-flux approach in GCMs. Some recent studies (e.g., Giangrande et al., 2013; Kumar et al., 2015; Giangrande et al., 2016) used wind profiler retrievals to attain long-term measurements. A limitation of these studies is the set of assumptions made to use observations at a point location to describe mass-flux at the scale of a GCM grid-box. To overcome this limitation, a later study from Kumar et al. (2016) proposed a parametric equation of vertical velocity inside convective updrafts as a function of radar reflectivity products: the 0-dBZ echo top height (ETH) and the height-weighted reflectivity index (Z_{HWT}). The present work makes use of this parametric approach to determine mass-flux and, in turn, the rate of mixing between the updraught and the environment (entrainment/detrainment) (Arakawa et al., 1974).

Observations on a scale of 100 km from a scanning C-band dual-polarisation radar (CPOL; Keenan et al. (1998)) in Darwin, are used in this paper. The Darwin region experiences a tropical climate with a dry and a wet season, the latter typically starts in late November or early December and lasts until late April. The brings with it heavy monsoonal downpours and cyclone activity. Its unique topography and the availability of a comprehensive long-term observational record, make the Darwin region an ideal location to study different regimes of tropical convection (Kumar et al., 2012; Davies et al., 2013; Kumar et al., 2015, 2016).

The aim of this study is to provide observationally based profiles of convective mass-flux, net fractional entrainment and their constituents using the C-band dual-polarisation radar (CPOL; Keenan et al. (1998)). With the quantities attained, a second goal is to investigate the relative role of area fraction and vertical velocity in determining the magnitude and shape of mass-flux profiles.

The article is organised as follows. In section 2 the data set used for the study is introduced. Section 3 describes the mass-flux equation and the assumptions used to de-

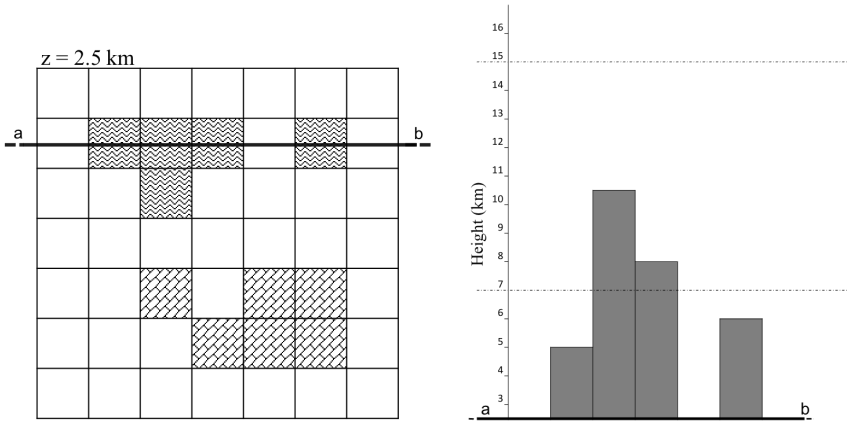

Figure 1. Schematic representation of a scene. The left panel shows three groups of rainy pixels (clouds) classified at $z_b = 2.5$ km: two are convective (wavy patter) and one is classified as stratiform (brick pattern). On the right panel a cross section taken within the convective clouds shows the vertical extent of convective pixels from 2.5 km to the respective 0-dBZ echo top height. The dashed lines mark the 7 and 15 km levels.

rive this quantity. Section 4 presents the main results of the analysis for the full data set (sections 4.1 and 4.2) and for composites of radar scenes with different cloud top heights (section 4.3).

2 Data

This study uses 13 wet seasons of data gathered by a C-Band Polarimetric radar (CPOL) located near Darwin, Australia (12.25°S, 131.04°E) (Keenan et al., 1998). The measurements cover the period of October 2001 to April 2015, with a gap in 2008, when the radar antenna and receiver needed replacement.

Measurements are available with a time resolution of 10 minutes, which is the time needed for the radar to perform a full three-dimensional scan. In this work each full radar scan will be referred to as a scene. Only measurements within the range $20 - 120km$ from the radar location are considered. This accounts for both the cone of silence around the radar and minimises any range-dependence issues far away from the radar (Kumar et al., 2013). The data is interpolated onto a three-dimensional regular grid with a 2.5 km x 2.5 km horizontal spacing and 0.25 km vertical spacing (Δz) ranging from 2.5 km to 13.5 km above the surface.

For each vertical column defined by the grid, the data set includes:

a) *A convective/stratiform classification for each rainy grid point.* Radar pixels are classified as either convective or stratiform using the algorithm of Steiner et al. (1995). This method classifies pixels with large values of radar reflectivity at 2.5 km height as convective. It also classifies sufficiently intense precipitation next to a convective pixel as convective. Other precipitating radar pixels are classified as stratiform. The left panel of Figure 1 helps visualising the outcome of this classification in an simplified gridded domain. The wavy pattern is for convective pixels and the brick pattern is for stratiform pixels. This study makes use of the convective pixel information only.

b) *The 0-dBZ echo top height* (ETH). This is the height where 0 dBZ at the top of a column of consecutive reflectivity values greater than zero is reached. This has been

shown to be a reasonable proxy of cloud top height as demonstrated by Casey et al. (2012) and Kumar et al. (2013). Convective columns, a proxy for convective clouds, are then defined as the vertical region from 2.5 km above the surface to the 0-dBZ height for each convective pixel. This is visualised in the right panel of Figure 1.

c) *The height-weighted reflectivity index (Z_{HWT}).* Kumar et al. (2016) found that the intensity of convection, expressed through the vertical velocity in convective drafts, is strongly related to a vertical integral measure of radar reflectivity in convective pixels. They defined a height-weighted index as

$$Z_{HWT} = \log_{10} \sum_k Z \cdot z_k, \tag{1}$$

where Z is the radar reflectivity and z is the height in km. Compared to a simple sum of the reflectivity in linear units, Z_{HWT} results to be better linked to vertical velocity throughout the evolution of a convective cell. The height-weighting in equation (1) gives additional weight to the upper part of updrafts, in which velocities tend to be stronger, while reflectivities tend to be lower due to the presence of ice.

As a key goal of this work is to study vertical profiles of convective mass-flux (see below), only scenes where convection occurs in at least one pixel and covers at least two vertical layers are chosen for analysis. It is worth noting that the CPOL radar only detects precipitation-size particles. As a result, non-precipitating clouds are not included in the analysis and all results relate to precipitating convection only.

3 Estimation of convective mass-flux

The goal of this study is to use the observations described above to estimate bulk mass-flux profiles for every convective scene in the data set. For simplicity, downdrafts are disregarded so that the resulting mass-flux only refers to positive upward vertical velocities inside convection. As the data set provides a very high time resolution of ten minutes, sequences of radar scenes will not be independent of each other. As this is a first attempt at exploiting the radar record to study mass-flux characteristics, a simple diagnostic approach is used, that is each scene is treated as independent and information about the life cycle of convective cells is not taken into account. This matches common practice in cumulus parametrisations used in weather and climate models. As mass-fluxes cannot be directly measured, the present study applies the approach proposed by Kumar et al. (2016), in which the mass-flux is computed from observational estimates of area fraction and vertical velocity within each radar scene, as

$$M_t(z) = \rho(z) w_t(z) a_t(z), \tag{2}$$

where $\rho(z)$ is the density, $w_t(z)$ is the vertical velocity averaged over all convective clouds (see below), and $a_t(z)$ is the fractional area of the radar scene that is covered by convective clouds. Note that the vertical velocity w and the cloud fraction a are functions of both height and time. Since the density ρ does not vary strongly with time we use a climatological time independent profile derived from a variational analysis algorithm (Zhang & Lin, 1997) applied to the ECMWF Interim Reanalysis (Dee et al., 2011) for the Darwin region (Davies et al., 2013; Louf et al., 2019). The estimation of area fraction and vertical velocity is described next.

3.1 Estimation of area fraction

The area fraction covered by convective clouds as a function of height is estimated by combining the results of the pixel rainfall classification algorithm with the estimate of cloud top height for each pixel. As discussed above, reflectivity at the lowest level (2.5

km height) for each radar scene is used to classify each pixel as either convective or stratiform using the algorithm by Steiner et al. (1995). Dividing the area of convective pixels by the total radar scene area provides the convective area fraction at the 2.5km-level.

Next, the 0-dBZ cloud top estimate for all convective pixels is used to determine the cloud depth at each individual convective pixel. It is worth noting that cloud depth can vary strongly from pixel to pixel. From the cloud-top information it is then straightforward to calculate the number of pixels that are convective at each height above the 2.5km-level and from that the convective area fraction as a function of height, $a_t(z)$. As the cloud top algorithm requires consecutive layers of reflectivity above the 0-dBZ threshold for a layer to be classified as cloud, the fractional area can only stay constant or decrease with height. Once more, it is important to remember that the area fraction refers only to grid cells where precipitating convection occurs and that grid cells with stratiform clouds do not contribute to the cloud fraction.

3.2 Estimation of updraft vertical velocity

To estimate the updraft vertical velocity a statistical model is applied that relates velocity to cloud depth and reflectivity, as proposed by Kumar et al. (2015, 2016). The model was developed using retrievals of in-cloud vertical motion from dual frequency wind-profiler observations within the CPOL radar domain (Williams, 2012). The main equations of the statistical model as it is applied here are presented below. For a detailed description, parameter estimation and evaluation of the statistical model the reader is referred to Kumar et al. (2016).

The model starts by using the 0-dBZ echo top height to classify convective pixels into three cumulus modes. It then assigns an idealised updraft wind profile shape (see equation (3)) to each radar pixel depending on its 0-dBZ echo top height.

The idealised updraft wind profiles for the three cumulus modes are defined as

$$w_{\mathrm{u}}(z) = \begin{cases} 0.404z + 0.9922, & \text{for ETH} \leq 7\text{km} \\ -0.0016z^4 + 0.0519z^3 - 0.571z^2 + 2.7z - 2.7351, & \text{for } 7 < \text{ETH} \leq 15\text{km} \\ -0.0454z^2 + 1.0889z - 0.8963 & \text{for ETH} > 15\text{km} \end{cases} \quad (3)$$

Having determined the shape of the vertical velocity profile as a function of echo top height at a single pixel, its magnitude needs to be estimated. This is achieved by scaling the profiles from equation (3) with a reflectivity-dependent scaling factor such that the vertical velocity at each convective pixel, i, and time, t, is given by:

$$w_{i,t}(z) = w_{\mathrm{u}}(z) T_Z(z). \quad (4)$$

The scaling factor, $T_Z(z)$, is expressed as

$$T_{\mathrm{z}}(z) = \left(\frac{w_{\mathrm{res}} + \overline{w}_{\mathrm{u}}}{\overline{w}_{\mathrm{u}}} \right) \left(\frac{w_{\mathrm{u}}(z)^{0.5}}{\overline{w}_{\mathrm{u}}^{0.5}} \right), \quad (5)$$

where $\overline{w}_{\mathrm{u}}$ is the column-mean updraft velocity estimated from equation (3). $\overline{w}_{\mathrm{u}}$ reads

$$\overline{w}_{\mathrm{u}} = \frac{\sum_k w_{\mathrm{u},k} \cdot \Delta z}{\mathrm{ETH} - z_{\mathrm{b}}}, \quad (6)$$

where the summation is over all discrete levels, spaced $\Delta z = 0.25$ km, from $z_{\mathrm{b}} =$ 2.5 km to ETH.

Importantly, a reflectivity-dependent velocity, w_{res} is introduced as

$$w_{\mathrm{res}} = a + bZ_{\mathrm{HWT}}, \tag{7}$$

where a and b are empirical coefficients and their formulation was suggested by Kumar et al. (2016) as $a = 4.3911 - 1.2381 \cdot \mathrm{ETH}$ and $b = -0.06064 + 0.02095 \cdot \mathrm{ETH}$, where ETH is expressed in km.

w_{res} quantifies the intuitive assumption that the vertical motion at convective pixels with larger reflectivity (note that a height-weighted integral of reflectivity is used) is likely stronger leading to more intense rainfall.

3.3 Estimation of the bulk mass-flux

Once a vertical velocity profile for each convective grid cell has been obtained using the method above, the bulk vertical velocity is calculated by averaging over all convective pixels at each height z to yield

$$w_t(z) = \frac{\sum_i w_{i,t}(z)}{N_{\mathrm{c}}(z)}, \tag{8}$$

where N_{c} is the number of convective pixels at height z.

Combining the result of equation (8) with the estimate of area fraction discussed in section 3.1 then allows the calculation of the bulk mass-flux, M_t, at every level using equation (2).

4 Results

4.1 Mass-flux and its components

Combining the estimates of area fraction and bulk vertical motion described in section 3 allows for the calculation of the bulk convective mass-flux for every 10-minute radar scene that contains convective pixels. Figure 2 shows the distribution of all components of the mass-flux as from equation (2). Panel (a) depicts the distribution of mass-flux M_t, (b) of the convective area fraction a_t, (c) of the bulk vertical velocity w_t and (d) of the product of density and vertical velocity $\rho \cdot w_t$. In each panel, the solid line depicts the mean value, the dashed line show the median and the dotted lines are the 25 and 75 percentiles of the total mass-flux distribution. Note that all percentiles are calculated separately for each vertical level and that the following set of equations hold at every level z:

$$\begin{aligned} \langle w \rangle &= \frac{\sum_{t=1}^{T} w_t a_t}{\sum_{t=1}^{T} a_t}, \\ \langle a \rangle &= \frac{1}{T} \sum_{t=1}^{T} a_t \quad , \\ \langle M \rangle &= \rho \langle w \rangle \langle a \rangle \end{aligned} \tag{9}$$

where the chevrons refer to the temporal average of a quantity and T is the total number of scenes.

The bulk mass-flux profiles (Figure 2a) show a well-known shape, with an increase in mass-flux at low levels, a peak at about 4-5 km above the surface followed by a steady decrease above that level (Yanai et al., 1973; Emanuel et al., 1994; Betts, 1975). The peak mean value of mass-flux is about $0.017\,\mathrm{kg\,m^{-2}\,s^{-1}}$. The distribution shows a pronounced skewness at all levels, with the median values being much smaller than the mean. The

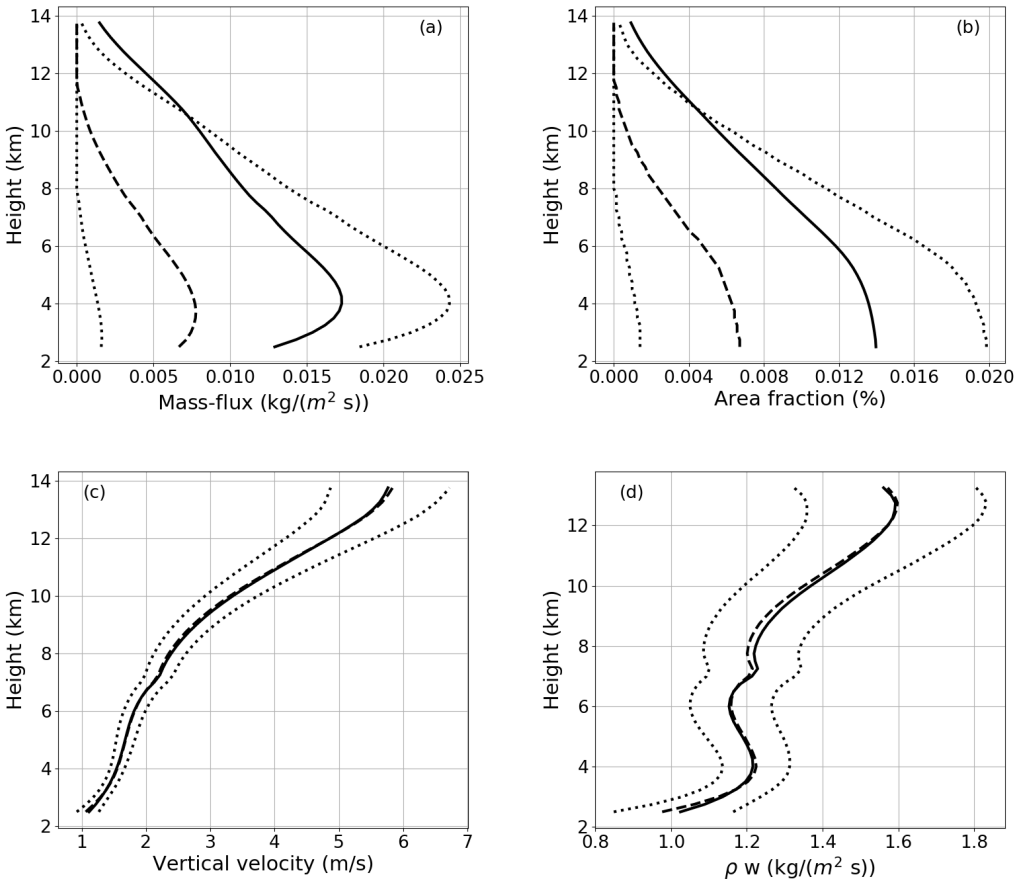

Figure 2. Temporal mean (solid), median (dashed), lower and upper quartiles (dotted) of bulk mass-flux (a), convective area fraction (b), bulk vertical velocity (c) and the product of density and bulk vertical velocity (d) for the entire data set.

peak median value is $0.0075\,\mathrm{kg\,m^{-2}\,s^{-1}}$ and it occurs slightly lower in the atmosphere than the peak mean value. The profile associated with the lower quartile indicates the prevalence of convective clouds with tops below 8 km and very weak mass-fluxes. The upper quartile shows a peak value near $0.025\,\mathrm{kg\,m^{-2}\,s^{-1}}$ with a more rapid decrease of mass-flux above the peak level than the mean or median. The pronounced skewness of the distribution suggests that, for the large majority of the radar scenes, mass-flux is small. The few occasions with very strong mass-fluxes skew the mean towards larger values. This confirms the well-known fact that strong convection is a sporadic occurrence (Houze Jr, 1973).

Decomposing the bulk mass-flux into contributions from the convective area fraction (Figure 2b) and bulk velocity (Figure 2c) provides a first insight into how the mass-flux profiles attain their distinct shape. First, it is evident that the skewness of the bulk mass-flux distribution is a result of a skewed distribution of convective area fraction, while for the vertical velocity median and mean values are almost identical.

It is worth remembering that, a decrease in area fraction indicates a loss of convective pixels with weak in-cloud vertical motion. Therefore, the increase of the bulk-vertical velocity with height is not only a result of in-cloud buoyancy (as would be the case for a single cloud) but also a result of fewer but stronger updraft that constitute the ensemble mean.

The increase in mass-flux below 4 km is associated with an increase in bulk vertical velocity. The convective area fraction is almost constant below 4 km, leading the in-cloud mass-flux ($\rho{\cdot}w$) to dominate the shape of the area average mass-flux. Between 4 and 6 km, the bulk vertical velocity does not increase significantly and the reduction of fractional area is more pronounced compared to lower levels. As a result, the mass-flux decreases with height in this 2 km layer. Above 6 km, both vertical velocity and in-cloud mass-flux are increasing with height. Nevertheless, a rapid decrease of bulk mass-flux is observed as a result of a rapid decrease in convective area fraction. This important characteristic of the observed cloud ensemble is a direct result of fewer and fewer clouds reaching the upper levels of the atmosphere. The small discontinuity at 7 km is a direct result of the vertical velocity model for different cloud depth (see equation (3)) not matching between cloud types at this level.

Given the large skewness of the bulk mass-flux distributions it is worth investigating its behaviour near the upper tail of the distribution. For this purpose Figure 3 shows the mean (solid line) and the 90th, 95th and 99th percentiles (dotted lines) of the bulk-mass-flux, convective area fraction and bulk vertical velocity. The figure also shows four individual profiles chosen as having the maximum mass-flux of all scenes at 2.5 km (blue), 5 km (red), 10 km (green) and 13.5 km (orange). The figure strongly supports the notion that it is the convective area fraction that largely determines the magnitude of the bulk mass-flux. For example, the scene with the strongest mass-flux at 2.5 km (blue line) also shows an exceptionally large area fraction at this level but its value of vertical velocity is not particularly strong.

There is also a noteworthy difference between the shape of the strongest bulk mass-flux profiles and those of the mean or median. Whereas the mean profile decreases with height, the strongest individual mass-flux profiles remain constant or even increase slightly with height. Figure 3 reveals that this is the result of an almost constant convective area fraction to a great depth in the atmosphere. The fact that this is not visible in the 95th or even 99th percentile of the distribution does indicate that this bulk mass-flux behaviour is very rare. Given the strong connection of bulk mass-flux to area average rainfall (Louf et al., 2019) these events are likely the most extreme rainfall events in the region (in an area average sense) and their difference in mass-flux behaviour warrants further study in the future.

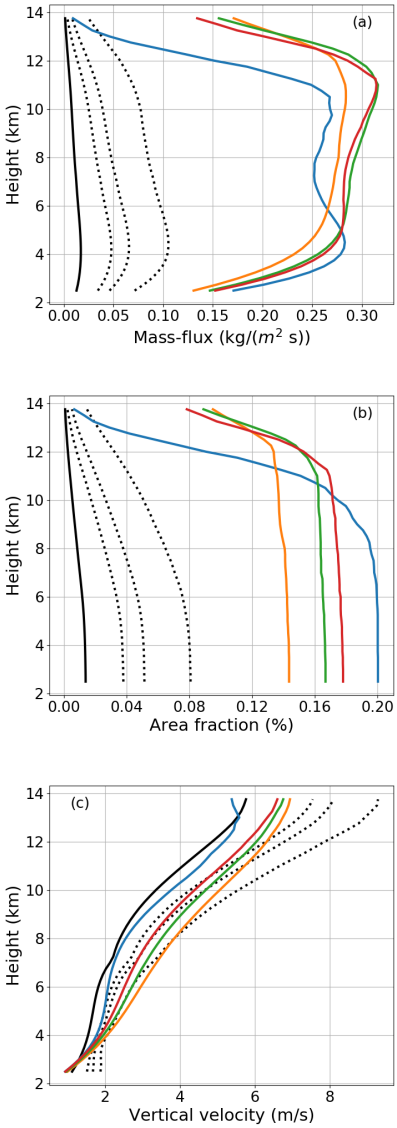

Figure 3. Temporal mean (black solid), 90th, 95th, 99th percentiles (black dotted) and the strongest mass-fluxes at various heights (see text). The three panels show bulk mass-flux (a), area fraction (b) and vertical velocity (c).

4.2 Vertical derivatives

To gain more insight into the vertical structure of the bulk-mass flux, the fractional change of the mass-flux with height can be related to the fractional change in area fraction and vertical velocity, using equation (2) as

$$\frac{1}{M_t}\frac{\partial M_t}{\partial z} = \frac{1}{a_t}\frac{\partial a_t}{\partial z} + \frac{1}{\rho w_t}\frac{\partial(\rho w_t)}{\partial z}. \tag{10}$$

In mass-flux models, the fractional change of mass-flux has been related to the fractional entrainment and detrainment rates, ϵ and δ, as (Tiedtke, 1989):

$$\frac{1}{M}\frac{\partial M}{\partial z} = \epsilon - \delta. \tag{11}$$

The fractional entrainment ϵ describes the inflow of environmental air into the cloudy updraft, while the fractional detrainment δ describes the outflow of cloudy air into the environment. Whereas there have been numerous studies that determined fractional entrainment and detrainment rates from numerical simulations (e.g. A. P. Siebesma et al. (1996); Lin et al. (1997); Carpenter et al. (1998)), to the best of our knowledge, there have been no direct observational estimates of the net effect of these mixing processes for deep convection. Applying equation (10) to the radar data set provides a first estimate of the net effect of these two processes based on long-term radar observations.

Using the date of the mass-flux, the area fraction and the vertical velocity, all three terms in equation (10) can be determined and their temporal averages are displayed in Figure 4. There are several distinct regions in the profile of the vertical derivative of the mass-flux (Figure 4(a)). Below roughly 4 km, the derivatives are positive. This is the result of a strongly positive vertical derivative of the vertical velocity term (Figure 4(c)), while the median of the vertical derivative of area fraction is zero in this region (Figure 4(b)). Above 4 km, the vertical derivative of the mass flux is negative. The derivative is fairly constant between five and ten kilometres and then increases in magnitude. This is is the result of a steadily strengthening negative vertical gradient in normalised area fraction, while the bulk vertical velocity gradients are small. We note once again that the spike observed at 7 km in Figure 4(c) is an artefact of the switching of calculation of the updraft vertical velocity for clouds deeper than 7 km from that for shallower ones (equation (3)). While this limits our interpretation of the vertical velocity evolution itself, the absence of a similar spike in the mass-flux derivative in Figure 4(a) demonstrates that the results for the overall mass-flux evolution are dominated by the much more directly observed convective area fraction.

As discussed above, the fractional change of mass-flux represents the net effect of entrainment and detrainment on the bulk mass-flux. (e.g., Tiedtke, 1989; A. P. Siebesma, 1996; de Rooy et al., 2012). When positive, there is net gain of mass in cloudy air through entrainment from the environment, while negative values indicate a net transfer of cloudy mass to the environment through detrainment. Our results show that, on average, convective cloud ensembles in the study area experience a strong and steady net entrainment from their base to about 4 km, moderate net detrainment between 4 and 10 km and strong net detrainment above 10 km. We note that this behaviour represents the entire cloud ensemble and is likely a combination of different behaviours of clouds of varying depth. To investigate this further, the next section will divide the data set into scenes that are characterised by clouds of different depth to investigate how different "cloud modes" might shape the overall mass-flux profile in Figure 2.

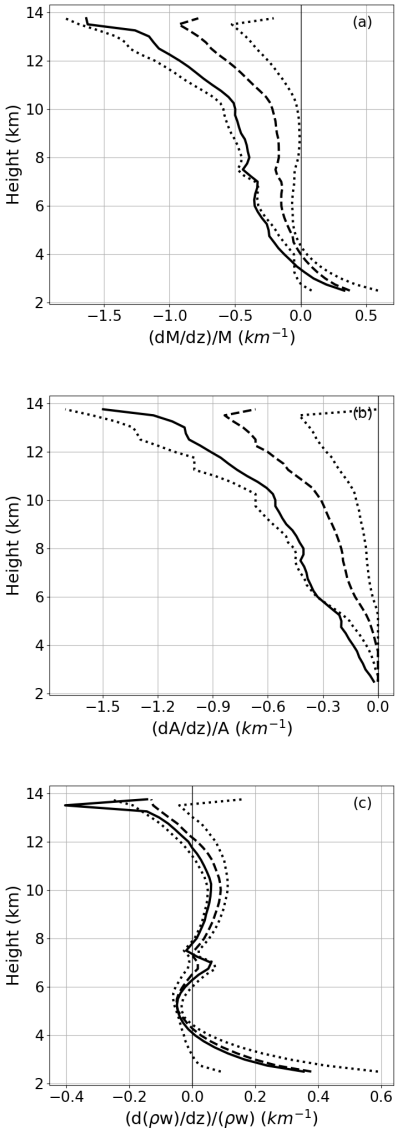

Figure 4. Temporal mean (solid), median (dashed), and upper and lower quartile (dotted) of the normalised vertical derivative of mass-flux (a), of area fraction (b) and of the product of density and vertical velocity (c) as a function of height.

4.3 Composite analysis by maximum Echo Top Height

We take advantage of the echo top height (ETH) information in our data set to divide the radar scenes based on the maximum echo top height (ETH_{max}) found in each of them. Following the study of Kumar et al. (2013) we choose the threshold values of 7 km and 15 km to define three classes of scenes: $ETH_{max} \leq 7km$, $7km < ETH_{max} \leq 15km$, and $ETH_{max} > 15km$. We then analyze the composite mass-flux behaviour for each of these three classes to see how they may shape the overall mass-flux profiles discussed above. We adopt the terminology of Kumar et al. (2013) and refer to these scenes as congestus, deep and overshooting. We use this nomenclature in a loose sense and note that unlike in Kumar et al. (2013), who classified individual clouds in this way, we assign the name to an entire scene if the maximum height reached by any cloud in the scene fulfils the criterion that defines the class.

Figure 5 shows the ETH distributions for all convective pixels for the entire data set (Figure 5(a)) and for three sub-groups of scenes selected based on the maximum ETH found in them (Figure 5(b-d)). The overall ETH distribution (Figure 5(a)) is quite broad with ETH between 6 and 12 km almost equally likely. There are small peaks at 7 and 9 km, respectively. Selecting scenes where the maximum ETH in the scene is below 7 km by definition eliminates all pixels with higher ETH. 21% of the scenes in our data set fall into this category. They represent relatively shallow congestus cloud fields. We note that these clouds still contain sufficient precipitation to be detected by the radar and should not be confused with non-precipitating shallow cumulus clouds, which are not detectable by the radar. The ETH distribution for the congestus class shows a rapid decrease of cloud top likelihood from the minimum detectable value (2.5 km) to the maximum (7km) (Figure 5(b)). This is consistent with a strong reduction of cloud area with height that is frequently reported in shallow cumulus fields (Brown et al., 2002; A. P. Siebesma et al., 2003; VanZanten et al., 2011), which according to our results translates to congestus cloud fields as well.

The shape of the distribution of deep convective cloud fields is very similar to the overall distribution except for the drop-off in likelihood which occurs at lower ETH and the lack of clouds deeper that 15 km, which has been introduced by the definition of deep convective scenes (Figure 5(c)). This similarity is in large part due to the fact that 63% of all scenes fall into this category. Remarkably, while by definition the maximum ETH in the scene is above 7 km, the distribution still peaks at 7 km. This indicates that even in cloud fields that contain deep convection, the most frequently observed clouds in the scene have moderate ETH between 6 and 8 km.

Scenes that contain overshooting convection constitute 16% of the total data set. The ETH distribution in the presence of overshooting clouds is distinctly different from all other categories (Figure 5(d)). The maximum likelihood of ETH shifts upward to values between 12 and 13 km, indicating the presences of a relatively large number of deep clouds (Figure 3). These scenes therefore represent the most wide-spread vigorous deep convection found in our data set.

Having separated all radar scenes into maximum ETH categories, we now analyse the vertical structure of the mass-flux, its components and their vertical derivatives (Figure 6). Each class of radar scenes is represented by the same colours used in Figure 5. There is a very clear separation in mass-flux strength between the categories (Figure 6(a)). The congestus class is characterised by very small mass-fluxes while scenes with overshooting convection show very large mass-fluxes. The deep class shows moderate values of mass-flux. It is evident that the main difference between classes comes from the convective area fraction (Figure 6(b)), while the updraft velocities (Figure 6(c)) are of similar order of magnitude in all classes, with the overshooting class showing values roughly 1 m/s larger than those for the deep class.

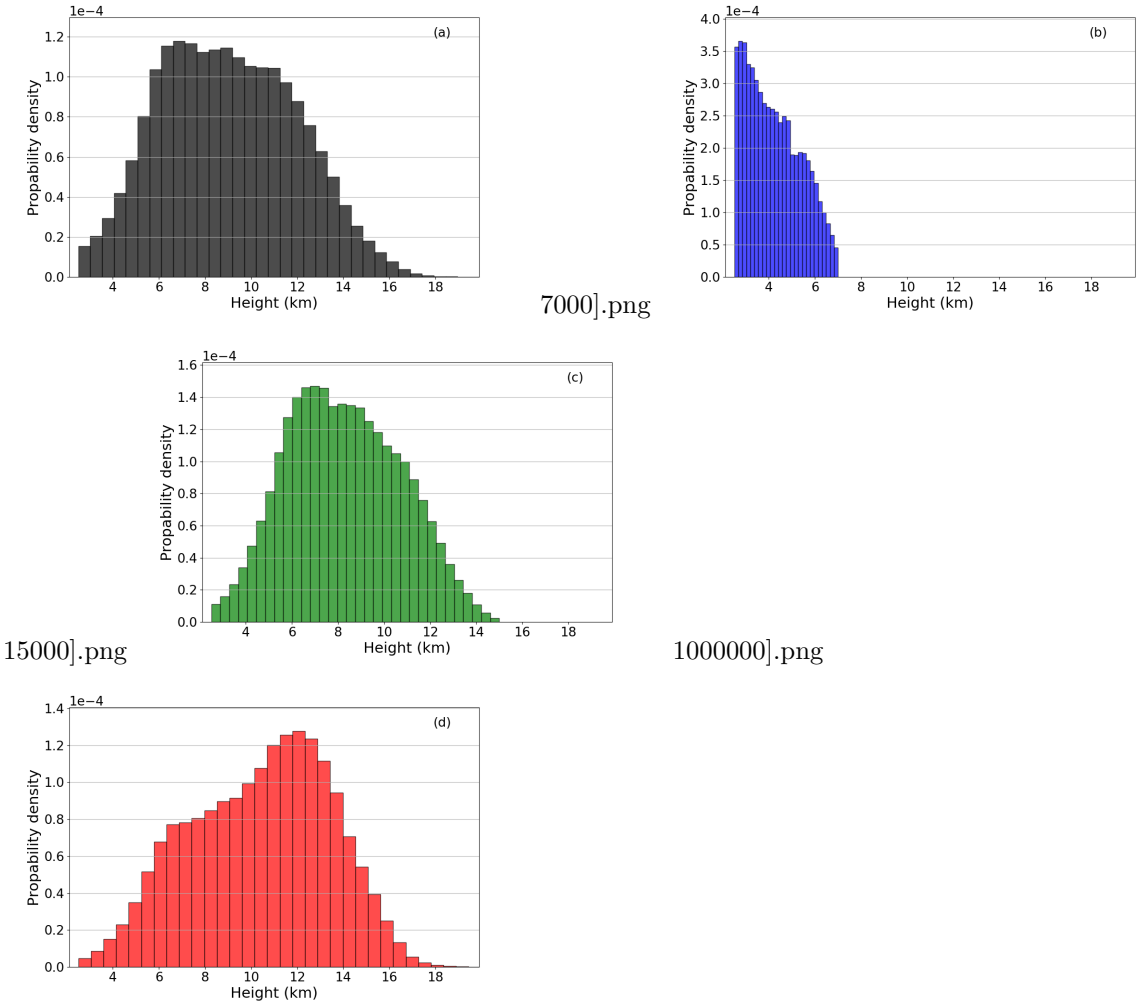

Figure 5. Frequency distribution of 0-dBZ ETH, used as a proxy for the height of convection in a pixel. In (a) all scenes of the data set are used, (b) refers to scenes where the tallest convective cell is lower than 7 km: Composite 1, (c) is obtained using scenes with the maximum extent of convection between 7 and 15 km: Composite 2, (d) is obtained from scenes with convective cells rising taller than 15 km: Composite 3.

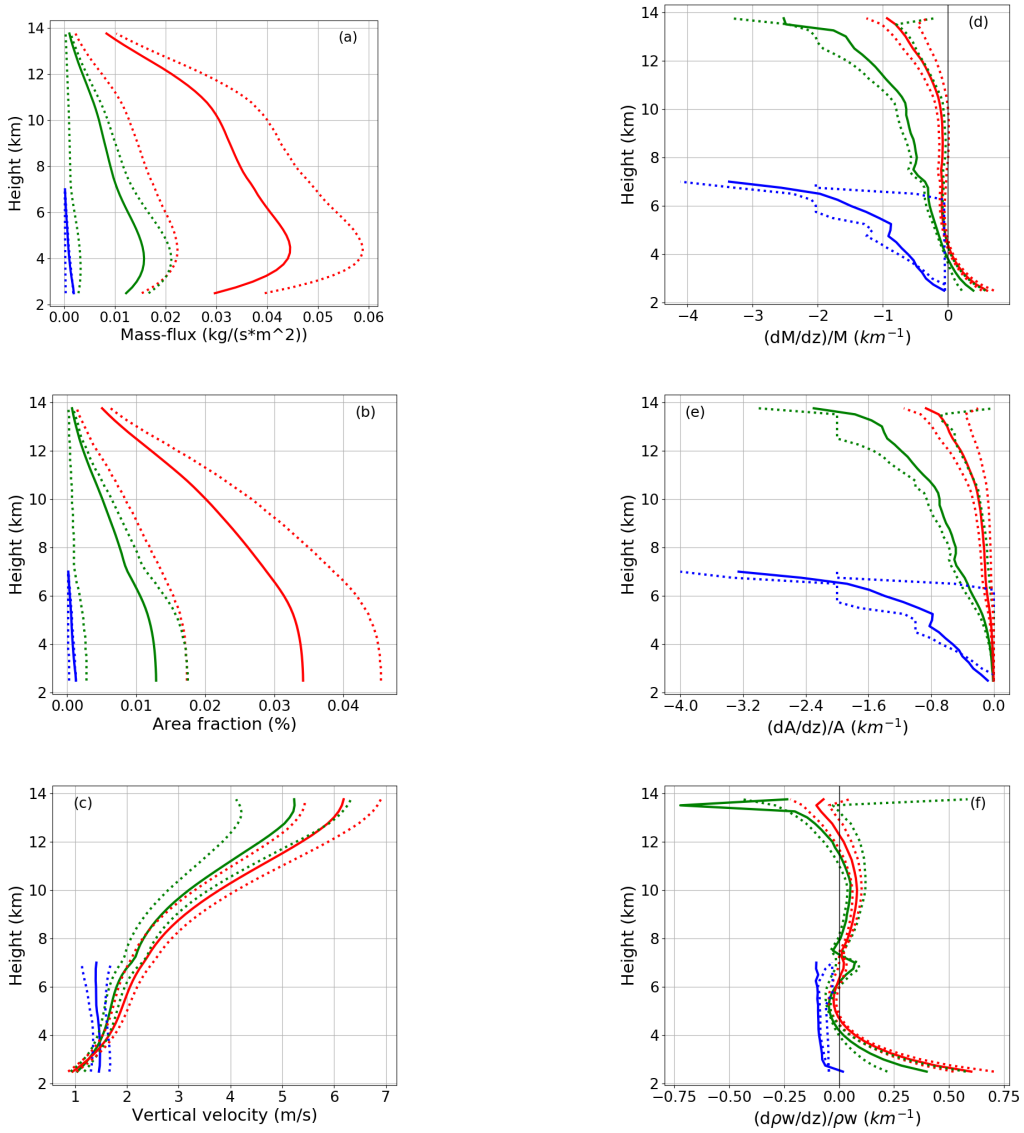

Figure 6. Vertical profiles of bulk mass-flux (a), area fraction (b) and vertical velocity (c) as well as their normalised vertical derivatives (d-f) for the congestus (blue), deep (green) and overshooting (red) classes of radar scenes. Solid lines indicate the median and dashed lines the 25th and 75th percentile, respectively.

There are notable differences in the vertical structure of mass-flux between the three classes. In congestus convection, the maximum mass flux is found at the lowest level in the data set (2.5 km) and is decreasing with height at all levels above with a rate that increases with height (Figure 6(d)). Once again, this behaviour is largely the result of a rapid decrease of area fraction with height (Figure 6(e)) accompanied by a weakly decreasing velocity component (Figure 6(f)). For both deep and overshooting convection, the mass-flux increases with height below 4 km with a larger rate found in overshooting convection. This larger rate of mass-flux increase at low levels is the result of larger rates of increase in the vertical velocity component, while the vertical derivatives of area fraction are close to zero for both deep and overshooting cases. Above 4 km the verti-

cal derivative of mass-flux is negative for both deep and overshooting convection mostly owing to negative derivatives for area fraction. Notably, the values for deep convection are several times larger than those for overshooting convection, indicating a more rapid decrease of mass-flux in the middle to upper troposphere. The apparent acceleration of the updrafts between 8 and 12 km is also slightly larger in the overshooting case. We note again that this "acceleration" in the bulk velocity is likely the result of the loss of weaker clouds from the ensemble and does not necessarily indicate an increase of velocity in individual clouds.

5 Conclusions

The aim of this study was to derive convective mass-fluxes and their constituents on the scale of a GCM grid-box from a C-band polarimetric radar and thereafter investigate the relative role of area fraction and vertical velocity in determining mass-flux. We made use of observational estimates of mass-flux spanning 13 wet seasons in the tropical region of Darwin. To the authors' knowledge, this is the first time that such long-standing measurements are exploited to retrieve a climatology of mass-flux. The exceptionally comprehensive data set allowed to elucidate on the statistical distribution of these profiles.

The analysis showed that, in this area, the ensemble mass-flux of precipitating convective clouds peaks at 4 km. Its distribution is positively skewed with the tail highlighting the presence of rare but very strong mass-fluxes. It was also found that the skewed distribution and the magnitude of mass-flux are largely determined by the fractional area covered by convection, while the in-cloud vertical velocity plays a less significant role. A similar result was reported in a study by Kumar et al. (2015) where it is stated that mass-flux is most strongly regulated by area fraction, although vertical velocity revealed non-negligible properties related to cloud dynamics. These results encourage parameterization methods that aim to estimate area fraction and vertical velocity separately (de Rooy & Pier Siebesma, 2010; Peters et al., 2013, 2017; A. Siebesma et al., 2020). Our results also suggested that, in a cloud ensemble, information on the vertical rate of change of the area fraction can reduce the need for parameterizing detrainment.

Figure 7 summarises the results of this study showing together the mean vertical derivatives of mass-flux (solid), area fraction (dash-dot) and in-cloud mass-flux (dash). The reader is reminded of equation (10) which implies that the solid line in Figure 7 results from combining the dashed line with the dash-dotted line. Each panel includes profiles from all scenes (black) and one of the three classes of scenes defined in section 4.3: congestus (blue), deep (green), overshooting (red).

All panels prove that the vertical rate of change of mass-flux (solid) mimics the vertical rate of change of convective area fraction (dash-dot), except for the layer below 4 km in scenes with deep or overshooting clouds. By separating the data set into composites according to the tallest convective cell, it was possible to demonstrate that the most common cloud field (63% of the scenes) presents the maximum 0-dBz ETH between 7 and 15 km. Remarkably, even in such cloud fields, containing deep convection, the most frequently observed clouds have moderate ETH between 6 and 8 km.

An analysis of the normalised vertical derivative of mass-flux further allowed to elucidate on the mixing process of clouds with the environment (i.e. net entrainment or net detrainment). In fact, positive values in Figure 7 indicate net fractional entrainment while negative values correspond to net fractional detrainment. From the considered ensembles of precipitating convective clouds it is possible to distinguish two regions in the vertical dimension: the first, below 4 km, is dominated by net fractional entrainment; the second, above 4 km, is dominated by net fractional detrainment. The region above 4 km

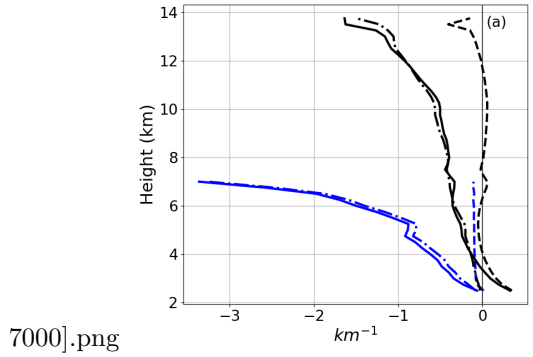

7000].png

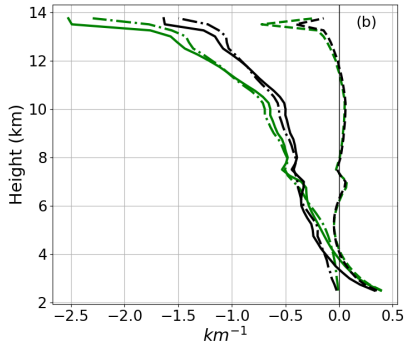

15000].png

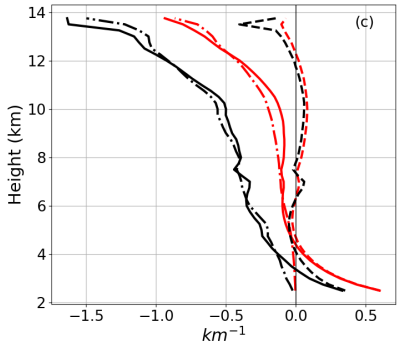

1000000].png

Figure 7. For each composite (Composite 1 (a), Composite 2 (b), Composite 3 (c)), mean profiles of all terms in equation (10) compared with means attained using all scenes (black lines). Solid line refers to $\frac{1}{M}\frac{\partial M}{\partial z}$, dash-dot line refers to $\frac{1}{A}\frac{\partial A}{\partial z}$, dashed line refers to $\frac{1}{\rho w}\frac{\partial \rho w}{\partial z}$.

is further divided into two layers. From 4 to 10 km an intermediate reduction rate of mass-flux is observed, while above 10 km mass-flux reduces more rapidly.

As this is a first attempt at characterising mass-flux from radar reflectivities, we adopted a simple bulk approach where all convective cells in the field are lumped together and the profiles of the ensemble are studied. Although this approach does not provide information on single clouds and their individual mass-flux profiles, the bulk approach was chosen because it is widely used in current GCMs. Furthermore, the methods of this work do not exclude the possibility of performing a similar analysis with a spectral approach. In fact, CPOL radar data are spatially distributed and individual clouds can be identified within a scene (Kumar et al., 2013; Louf et al., 2019).

Despite the great potential of deriving mass-flux from radar reflectivity, this study is based on a single radar location and further investigation is needed before extending our conclusions to other regions of the Earth. Future works should also focus on accounting for the effect of non-precipitating convection as this can sensibly alter the total mass-flux of a cloud field, especially in what we called congestus scenes.

Acknowledgments

We would like to acknowledge the contribution of Louise Nuijens. The radar data set used in this study was provided by Valentin Louf and it is available in the Atmospheric Radiation Measurement program archive (https:// www.arm.gov/). Christian Jakob acknowledges funding from The Australian Research Councils Centre of Excellence for Climate Extremes (CE170100023).

References

Anderson, N. F., Grainger, C. A., & Stith, J. L. (2005, may). Characteristics of Strong Updrafts in Precipitation Systems over the Central Tropical Pacific Ocean and in the Amazon. *Journal of Applied Meteorology*, *44*(5), 731–738. Retrieved from `http://journals.ametsoc.org/doi/10.1175/JAM2231.1` doi: 10.1175/JAM2231.1

Arakawa, A. (2004, jul). The cumulus parameterization problem: Past, present, and future. *Journal of Climate*, *17*(13), 2493–2525. Retrieved from `http://journals.ametsoc.org/doi/abs/10.1175/1520-0442{\%}282004{\%}29017{\%}3C2493{\%}3ARATCPP{\%}3E2.0.CO{\%}3B2` doi: 10.1175/1520-0442(2004)017⟨2493:RATCPP⟩2.0.CO;2

Arakawa, A., Schubert, W. H., Arakawa, A., & Schubert, W. H. (1974, apr). Interaction of a Cumulus Cloud Ensemble with the Large-Scale Environment, Part I. *Journal of the Atmospheric Sciences*, *31*(3), 674–701. Retrieved from `http://journals.ametsoc.org/doi/abs/10.1175/1520-0469{\%}281974{\%}29031{\%}3C0674{\%}3AIOACCE{\%}3E2.0.CO{\%}3B2` doi: 10.1175/1520-0469(1974)031⟨0674:IOACCE⟩2.0.CO;2

Bechtold, P., Koehler, M., Jung, T., Doblas-Reyes, F., Leutbecher, M., Rodwell, M. J., ... Balsamo, G. (2008). Advances in simulating atmospheric variability with the ECMWF model: From synoptic to decadal time-scales. *Quarterly Journal of the Royal Meteorological Society*, *134*(634), 1337 – 1351. Retrieved from `http://dx.doi.org/10.1002/qj.289` doi: 10.1002/qj.289

Betts, A. K. (1975). Parametric interpretation of trade-wind cumulus budget studies. *Journal of Atmospheric Sciences*, *32*(10), 1934–1945.

Brown, A., Cederwall, R., Chlond, A., Duynkerke, P., Golaz, J.-C., Khairoutdinov, M., ... others (2002). Large-eddy simulation of the diurnal cycle of shallow cumulus convection over land. *Quarterly Journal of the Royal Meteorological Society: A journal of the atmospheric sciences, applied meteorology and physical oceanography*, *128*(582), 1075–1093.

Byers, H. R., & Braham, R. R. (1949). The thunderstorm: report of the Thunderstorm Project. *US Government Printing Office*.

Carpenter, R., Droegemeier, K., & Blyth, A. M. (1998, dec). Entrainment and Detrainment in Numerically Simulated Cumulus Congestus Clouds. Part II: Cloud Budgets. *http://dx.doi.org/10.1175/1520-0469(1998)055<3433:EADINS>2.0.CO;2*. doi: 10.1175/1520-0469(1998)055⟨3433:EADINS⟩2.0.CO;2

Casey, S. P. F., Fetzer, E. J., & Kahn, B. H. (2012, feb). Revised identification of tropical oceanic cumulus congestus as viewed by CloudSat. *Atmospheric Chemistry and Physics*, *12*(3), 1587–1595. Retrieved from https://www.atmos-chem-phys.net/12/1587/2012/ doi: 10.5194/acp-12-1587-2012

Davies, L., Jakob, C., May, P., Kumar, V. V., & Xie, S. (2013, oct). Relationships between the large-scale atmosphere and the small-scale convective state for Darwin, Australia. *Journal of Geophysical Research Atmospheres*, *118*(20), 11534–11545. Retrieved from http://doi.wiley.com/10.1002/jgrd.50645 doi: 10.1002/jgrd.50645

Dee, D. P., Uppala, S. M., Simmons, A. J., Berrisford, P., Poli, P., Kobayashi, S., ... Vitart, F. (2011, apr). The ERA-Interim reanalysis: configuration and performance of the data assimilation system. *Quarterly Journal of the Royal Meteorological Society*, *137*(656), 553–597. Retrieved from http://doi.wiley.com/10.1002/qj.828 doi: 10.1002/qj.828

de Rooy, W. C., Bechtold, P., Fröhlich, K., Hohenegger, C., Jonker, H., Mironov, D., ... Yano, J. I. (2012). Entrainment and detrainment in cumulus convection: An overview. *Quarterly Journal of the Royal Meteorological Society*, *139*(670), 1–19. doi: 10.1002/qj.1959

de Rooy, W. C., & Pier Siebesma, A. (2010). Analytical expressions for entrainment and detrainment in cumulus convection. *Quarterly Journal of the Royal Meteorological Society*. doi: 10.1002/qj.640

de Rooy, W. C., Siebesma, A. P., de Rooy, W. C., & Siebesma, A. P. (2008, feb). A Simple Parameterization for Detrainment in Shallow Cumulus. *Monthly Weather Review*, *136*(2), 560–576. Retrieved from http://journals.ametsoc.org/doi/abs/10.1175/2007MWR2201.1 doi: 10.1175/2007MWR2201.1

Emanuel, K. A., David Neelin, J., & Bretherton, C. S. (1994, jul). On large-scale circulations in convecting atmospheres. *Quarterly Journal of the Royal Meteorological Society*, *120*(519), 1111–1143. Retrieved from http://doi.wiley.com/10.1002/qj.49712051902 doi: 10.1002/qj.49712051902

Giangrande, S. E., Collis, S., Straka, J., Protat, A., Williams, C., & Krueger, S. (2013, oct). A Summary of Convective-Core Vertical Velocity Properties Using ARM UHF Wind Profilers in Oklahoma. *Journal of Applied Meteorology and Climatology*, *52*(10), 2278–2295. Retrieved from http://journals.ametsoc.org/doi/10.1175/JAMC-D-12-0185.1 doi: 10.1175/JAMC-D-12-0185.1

Giangrande, S. E., Toto, T., Jensen, M. P., Bartholomew, M. J., Feng, Z., Protat, A., ... Machado, L. (2016, nov). Convective cloud vertical velocity and massflux characteristics from radar wind profiler observations during GoAmazon2014/5. *Journal of Geophysical Research: Atmospheres*, *121*(21), 12,891–12,913. Retrieved from https://onlinelibrary.wiley.com/doi/abs/10.1002/2016JD025303 doi: 10.1002/2016JD025303

Gregory, D., & Rowntree, P. R. (1990). A Mass Flux Convection Scheme with Representation of Cloud Ensemble Characteristics and Stability-Dependent Closure. *Monthly Weather Review*, *118*(7), 1483 – 1506. Retrieved from http://dx.doi.org/10.1175/1520-0493(1990)118<1483:AMFCSW>2.0.CO;2 doi: doi:10.1175/1520-0493(1990)118⟨1483:AMFCSW⟩2.0.CO;2

Houze Jr, R. A. (1973). A climatological study of vertical transports by cumulus-scale convection. *Journal of Atmospheric Sciences*, *30*(6), 1112–1123.

Jackson, R. C., Collis, S. M., Louf, V., Protat, A., & Majewski, L. (2018). A 17 year climatology of the macrophysical properties of convection in Darwin. *Atmospheric Chemistry and Physics*, *18*(23), 17687–17704. Retrieved from https://acp.copernicus.org/articles/18/17687/2018/ doi: 10.5194/acp-18-17687-2018

Jakob, C. (2010, jul). Accelerating progress in global atmospheric model development through improved parameterizations: Challenges, opportunities, and strategies. *Bulletin of the American Meteorological Society*, *91*(7), 869–875. doi: 10.1175/2009BAMS2898.1

Jr., R. A. H., Rasmussen, K. L., Zuluaga, M. D., & Brodzik, S. R. (2015). The Variable Nature of Convection in the Tropics and Subtropics: A Legacy of 16 Years of the Tropical Rainfall Measuring Mission (TRMM) Satellite. *Rev. Geophys.*, *53*(3), n/a – n/a. doi: 10.1002/2015rg000488

Keenan, T., Glasson, K., Cummings, F., Bird, T. S., Keeler, J., Lutz, J., ... Lutz, J. (1998, aug). The BMRC/NCAR C-Band Polarimetric (C-POL) Radar System. *Journal of Atmospheric and Oceanic Technology*, *15*(4), 871–886. Retrieved from http://journals.ametsoc.org/doi/abs/10.1175/1520-0426{\%}281998{\%}29015{\%}3C0871{\%}3ATBNCBP{\%}3E2.0.CO{\%}3B2 doi: 10.1175/1520-0426(1998)015⟨0871:TBNCBP⟩2.0.CO;2

Kumar, V. V., Jakob, C., Protat, A., May, P. T., & Davies, L. (2013, aug). The four cumulus cloud modes and their progression during rainfall events: A C-band polarimetric radar perspective. *Journal of Geophysical Research: Atmospheres*, *118*(15), 8375–8389. Retrieved from http://doi.wiley.com/10.1002/jgrd.50640 doi: 10.1002/jgrd.50640

Kumar, V. V., Jakob, C., Protat, A., May, P. T., & Williams, C. R. (2015). Mass-Flux Characteristics of Tropical Cumulus Clouds from Wind Profiler Observations at Darwin, Australia. *Journal of the Atmospheric Sciences*, *72*(5), 1837–1855. doi: 10.1175/jas-d-14-0259.1

Kumar, V. V., Protat, A., Jakob, C., Williams, C. R., Rauniyar, S., Stephens, G. L., & May, P. T. (2016). The estimation of convective mass flux from radar reflectivities. *Journal of Applied Meteorology and Climatology*, *55*(5), 1239–1257. doi: 10.1175/JAMC-D-15-0193.1

Kumar, V. V., Protat, A., May, P. T., Jakob, C., Penide, G., Kumar, S., & Davies, L. (2012, apr). On the Effects of Large-Scale Environment and Surface Types on Convective Cloud Characteristics over Darwin, Australia. *Monthly Weather Review*, *141*(4), 1358–1374. Retrieved from http://journals.ametsoc.org/doi/abs/10.1175/MWR-D-12-00160.1 doi: 10.1175/mwr-d-12-00160.1

Kummerow, C., Barnes, W., Kozu, T., Shiue, J., & Simpson, J. (1998). The Tropical Rainfall Measuring Mission (TRMM) sensor package. *J. Atmos. Oceanic Technol.*, *15*, 809 – 817.

Labbouz, L., Kipling, Z., Stier, P., Protat, A., Labbouz, L., Kipling, Z., ... Protat, A. (2018, may). How Well Can We Represent the Spectrum of Convective Clouds in a Climate Model? Comparisons between Internal Parameterization Variables and Radar Observations. *Journal of the Atmospheric Sciences*, *75*(5), 1509–1524. Retrieved from http://journals.ametsoc.org/doi/10.1175/JAS-D-17-0191.1 doi: 10.1175/JAS-D-17-0191.1

LeMone, M. A., & Zipser, E. J. (1980, nov). Cumulonimbus Vertical Velocity Events in GATE. Part I: Diameter, Intensity and Mass Flux. *http://dx.doi.org/10.1175/1520-0469(1980)037<2444:CVVEIG>2.0.CO;2*. doi: 10.1175/1520-0469(1980)037⟨2444:CVVEIG⟩2.0.CO;2

Lin, C., Arakawa, A., Lin, C., & Arakawa, A. (1997, apr). The Macroscopic Entrainment Processes of Simulated Cumulus Ensemble. Part II: Testing the Entraining-Plume Model. *http://dx.doi.org/10.1175/1520-0469(1997)054<1044:TMEPOS>2.0.CO;2*. doi: 10.1175/1520-0469(1997)054⟨1044:TMEPOS⟩2.0.CO;2

Louf, V., Jakob, C., Protat, A., Bergemann, M., & Narsey, S. (2019, aug). The Relationship of Cloud Number and Size With Their LargeScale Environment in Deep Tropical Convection. *Geophysical Research Letters*, *46*(15), 9203–9212. doi: 10.1029/2019gl083964

Marwitz, J. D. (1973, oct). Trajectories Within the Weak Echo Regions of Hailstorms. *http://dx.doi.org/10.1175/1520-0450(1973)012<1174:TWTWER>2.0.CO;2*. doi: 10.1175/1520-0450(1973)012⟨1174:TWTWER⟩2.0.CO;2

May, P. T., Mather, J. H., Vaughan, G., Jakob, C., McFarquhar, G. M., Bower, K. N., & Mace, G. G. (2008). The Tropical warm pool international Cloud Experiment. *Bulletin of the American Meteorological Society*. doi: 10.1175/BAMS-89-5-629

Nesbitt, S. W., Zipser, E. J., & Cecil, D. J. (2000). A census of precipitation features in the tropics using trmm: Radar, ice scattering, and lightning observations. *Journal of Climate*, *13*, 4087 – 4106.

Nitta, T. (1975, jan). Observational Determination of Cloud Mass Flux Distributions. *Journal of the Atmospheric Sciences*, *32*(1), 73–91. Retrieved from `http://journals.ametsoc.org/doi/abs/10.1175/1520-0469{\%}281975{\%}29032{\%}3C0073{\%}3AODOCMF{\%}3E2.0.CO{\%}3B2` doi: 10.1175/1520-0469(1975)032⟨0073:odocmf⟩2.0.co;2

Nitta, T., & Esbensen, S. K. (1974). Heat and moisture budget analyses using BOMEX data. *Monthly Weather Review*, *102*, 17 – 28.

Oerlemans, J. (1986). Convection in a conditionally unstable atmosphere: a reinvestigation of bjerknes' slice method. *Contributions to atmospheric physics*, *59*, 41-53.

Ooyama, K. (1971). A Theory on Parameterization of Cumulus Convection. *Journal of the Meteorological Society of Japan. Ser. II*, *49A*(0), 744–756. doi: 10.2151/jmsj1965.49a.0_744

Peters, K., Crueger, T., Jakob, C., & Möbis, B. (2017). Improved MJO-simulation in ECHAM6.3 by coupling a Stochastic Multicloud Model to the convection scheme. *Journal of Advances in Modeling Earth Systems*, *9*(1), 193–219. Retrieved from `http://doi.wiley.com/10.1002/2016MS000809` doi: 10.1002/2016MS000809

Peters, K., Jakob, C., & Davies, L. (2013). Stochastic behavior of tropical convection in observations and a multicloud model. *Journal of the Atmospheric Sciences*, *70*(11), 3556 – 3575. doi: 10.1175/jas-d-13-031.1

Riehl, H., & Malkus, J. S. (1958). On the heat balance in the equatorial trough zone. *Geophysica*(6), 503 – 538.

Riehl, H., & Malkus, J. S. (1979). The heat balance of the equatorial trough zone, revisited. *Contrib. Atmos. Phys.*(52,), 287–305.

Schalkwijk, J., Jonker, H. J. J., Siebesma, A. P., & Bosveld, F. C. (2015). A year-long large-eddy simulation of the weather over cabauw: An overview. *Monthly Weather Review*, *143*(3), 828 - 844. Retrieved from `https://journals.ametsoc.org/view/journals/mwre/143/3/mwr-d-14-00293.1.xml` doi: 10.1175/MWR-D-14-00293.1

Schemann, V., Ebell, K., Pospichal, B., Neggers, R., Moseley, C., & Stevens, B. (2020). Linking large-eddy simulations to local cloud observations. *Journal of Advances in Modeling Earth Systems*, *12*(12), e2020MS002209. Retrieved from `https://agupubs.onlinelibrary.wiley.com/doi/abs/10.1029/2020MS002209` (e2020MS002209 10.1029/2020MS002209) doi: https://doi.org/10.1029/2020MS002209

Schumacher, C., & Houze, R. A. (2003, jun). *Stratiform Rain in the Tropics as Seen by the TRMM Precipitation Radar ** (Vol. 16; Tech. Rep. No. 11). Retrieved from `http://daac.gsfc.nasa.gov/;` doi: 10.1175/1520-0442(2003)016⟨1739:SRITTA⟩2.0.CO;2

Siebesma, A., Bony, S., Jakob, c., & Stevens, B. (2020). Parameterising clouds. In *Clouds and climate: Climate science's greatest challenge* (p. 170217). Cambridge University Press. doi: 10.1017/9781107447738.007

Siebesma, A. P. (1996). *On the mass flux approach for atmospheric convection.* Shinfield Park, Reading: ECMWF. Retrieved from `https://www.ecmwf.int/node/12223`

Siebesma, A. P., Bretherton, C. S., Brown, A., Chlond, A., Cuxart, J., Duynkerke, P. G., ... others (2003). A large eddy simulation intercomparison study of shallow cumulus convection. *Journal of the Atmospheric Sciences*, *60*(10), 1201–1219.

Siebesma, A. P., Cuijpers, J. W. M., Siebesma, A. P., & Cuijpers, J. W. M. (1996, mar). Evaluation of Parametric Assumptions for Shallow Cumulus Convection. *http://dx.doi.org/10.1175/1520-0469(1995)052<0650:EOPAFS>2.0.CO;2*. doi: 10.1175/1520-0469(1995)052⟨0650:EOPAFS⟩2.0.CO;2

Simpson, J., Halverson, J. B., Ferrier, B. S., Petersen, W. A., Simpson, R. H., Blakeslee, R., & Durden, S. L. (1998). On the role of "hot towers" in tropical cyclone formation. *Meteorology and Atmospheric Physics*, *67*(1-4), 15–35. doi: 10.1007/BF01277500

Steiner, M., Houze, R. A., Yuter, S. E., Steiner, M., Jr., R. A. H., & Yuter, S. E. (1995, sep). Climatological Characterization of Three-Dimensional Storm Structure from Operational Radar and Rain Gauge Data. *Journal of Applied Meteorology*, *34*(9), 1978–2007. Retrieved from `http://journals.ametsoc.org/doi/abs/10.1175/1520-0450{\%}281995{\%}29034{\%}3C1978{\%}3ACCOTDS{\%}3E2.0.CO{\%}3B2` doi: 10.1175/1520-0450(1995)034⟨1978:CCOTDS⟩2.0.CO;2

Tiedtke, M. (1989). A comprehensive mass flux scheme for cumulus parameterization in large-scale models. *Monthly Weather Review*. doi: 10.1175/1520-0493(1989)117⟨1779:ACMFSF⟩2.0.CO;2

VanZanten, M. C., Stevens, B., Nuijens, L., Siebesma, A. P., Ackerman, A., Burnet, F., ... others (2011). Controls on precipitation and cloudiness in simulations of trade-wind cumulus as observed during rico. *Journal of Advances in Modeling Earth Systems*, *3*(2).

Wagner, T. M., & Graf, H. F. (2010). An ensemble cumulus convection parameterization with explicit cloud treatment. *Journal of the Atmospheric Sciences*. doi: 10.1175/2010JAS3485.1

Williams, C. R. (2012, oct). Vertical Air Motion Retrieved from Dual-Frequency Profiler Observations. *Journal of Atmospheric and Oceanic Technology*, *29*(10), 1471–1480. Retrieved from `http://journals.ametsoc.org/doi/abs/10.1175/JTECH-D-11-00176.1` doi: 10.1175/JTECH-D-11-00176.1

Yanai, M., Esbensen, S., Chu, J.-H., Yanai, M., Esbensen, S., & Chu, J.-H. (1973, may). Determination of Bulk Properties of Tropical Cloud Clusters from Large-Scale Heat and Moisture Budgets. *http://dx.doi.org/10.1175/1520-0469(1973)030<0611:DOBPOT>2.0.CO;2*. doi: 10.1175/1520-0469(1973)030⟨0611:DOBPOT⟩2.0.CO;2

Zhang, M. H., & Lin, J. L. (1997). Constrained variational analysis of sounding data based on column-integrated budgets of mass, heat, moisture, and momentum: Approach and application to ARM measurements. *Journal of the Atmospheric Sciences*. doi: 10.1175/1520-0469(1997)054⟨1503:CVAOSD⟩2.0.CO;2

Zipser, E. J. (2003). Some Views On "Hot Towers" after 50 Years of Tropical Field Programs and Two Years of TRMM Data. In W.-K. Tao & R. Adler (Eds.), *Cloud systems, hurricanes, and the tropical rainfall measuring mission (trmm): A tribute to dr. joanne simpson* (pp. 49–58). Boston, MA: American Meteorological Society. Retrieved from `https://doi.org/10.1007/978-1-878220-63-9{\_}5` doi: 10.1007/978-1-878220-63-9_5

Figure 1.

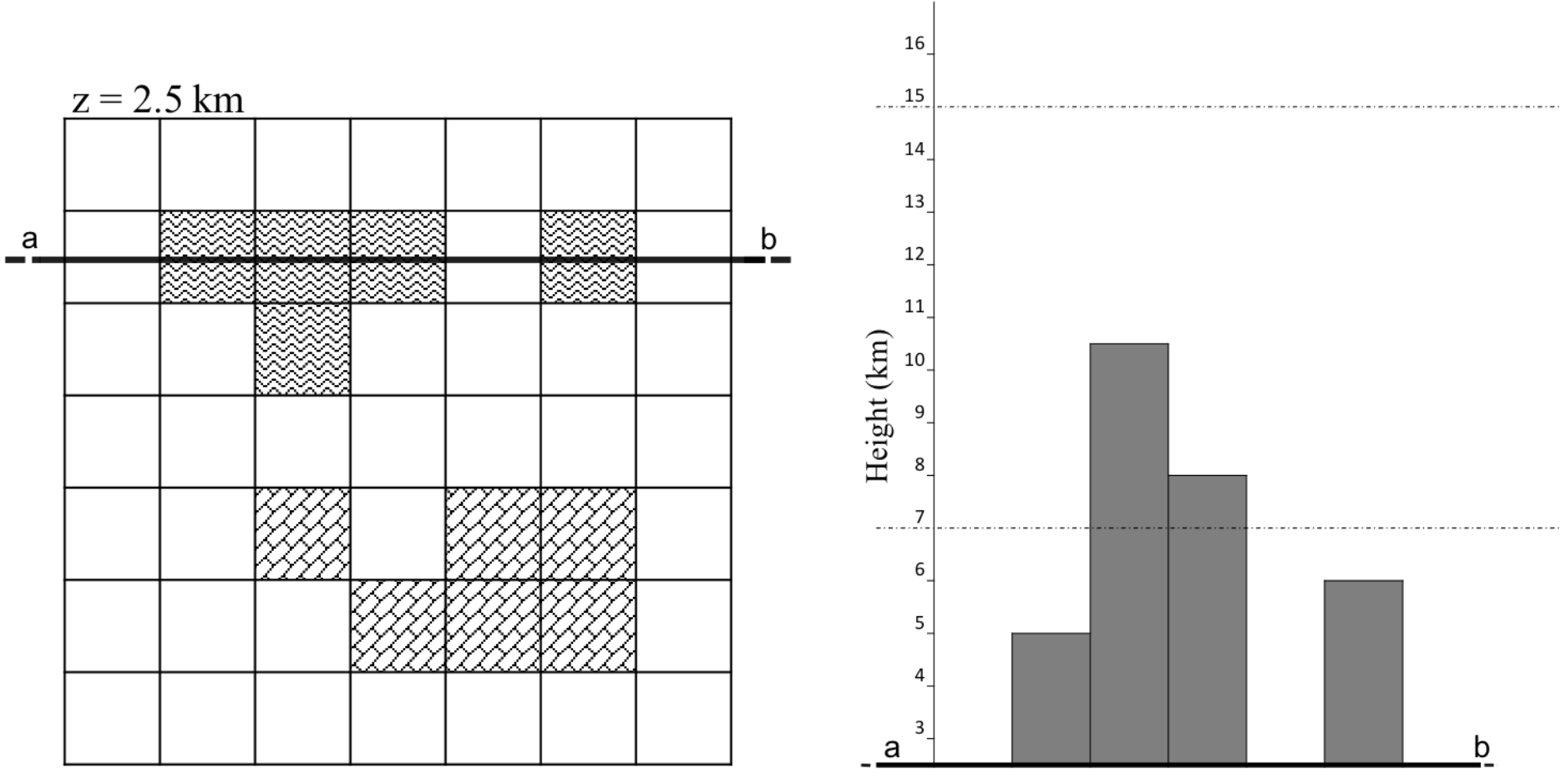
z = 2.5 km
a
b
Height (km)
16
15
14
13
12
11
10
9
8
7
6
5
4
3
a
b

Figure 2a.

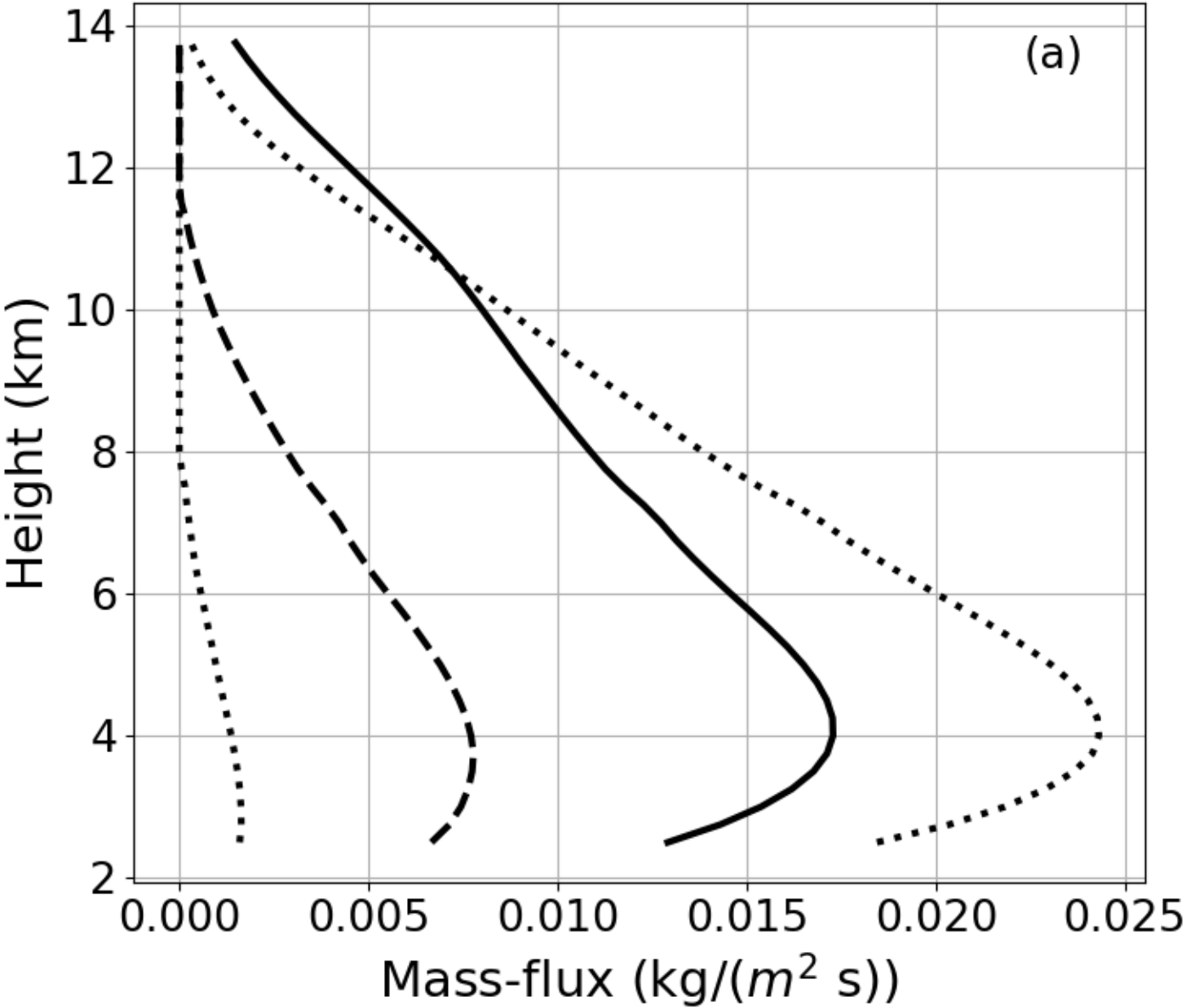
(a)
Height (km)
14
12
10
8
6
4
2
0.000
0.005
0.010
0.015
0.020
0.025
Mass-flux (kg/(m^2 s))

Figure 2b.

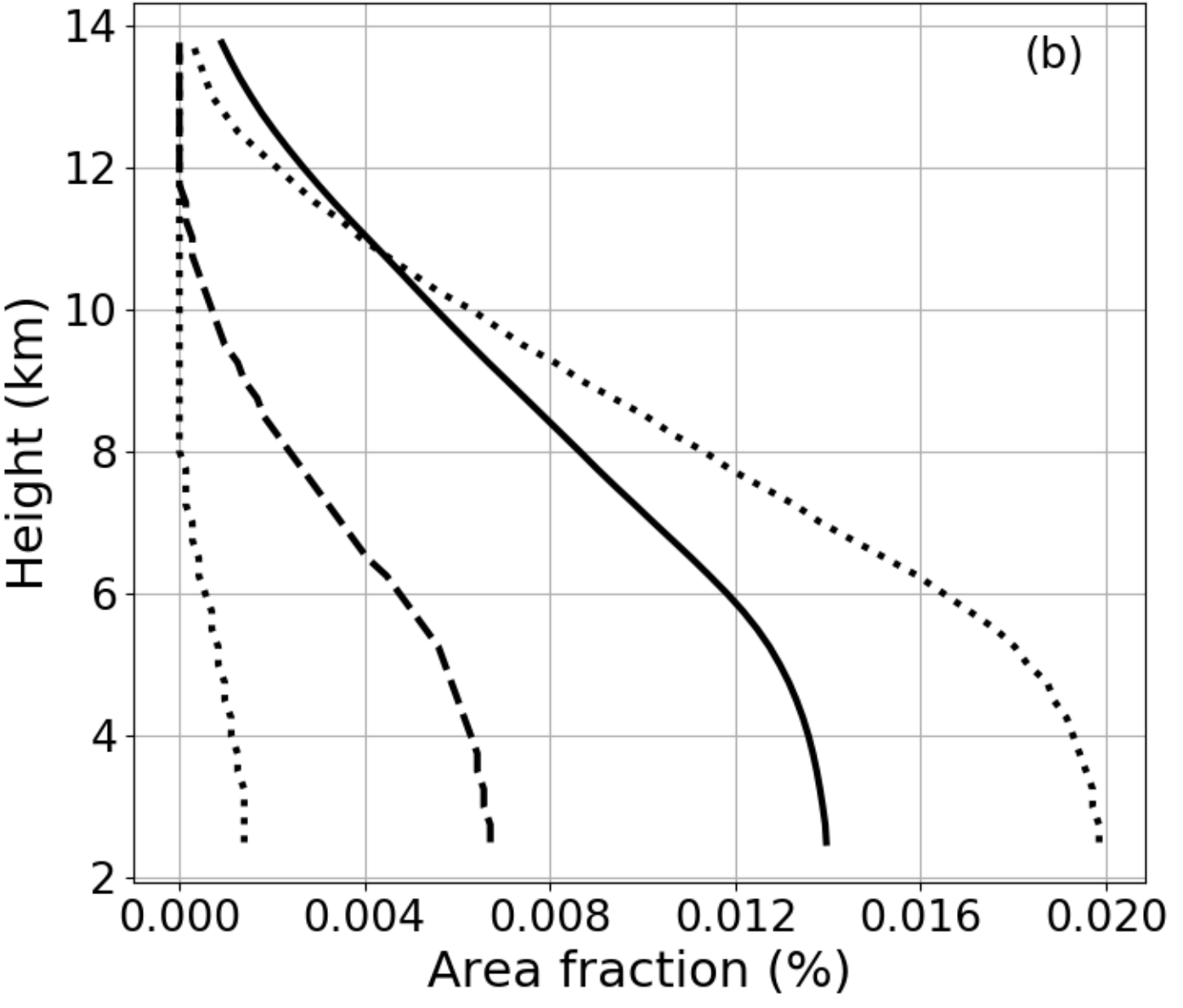
(b)
Height (km)
14
12
10
8
6
4
2
0.000
0.004
0.008
0.012
0.016
0.020
Area fraction (%)

Figure 2c.

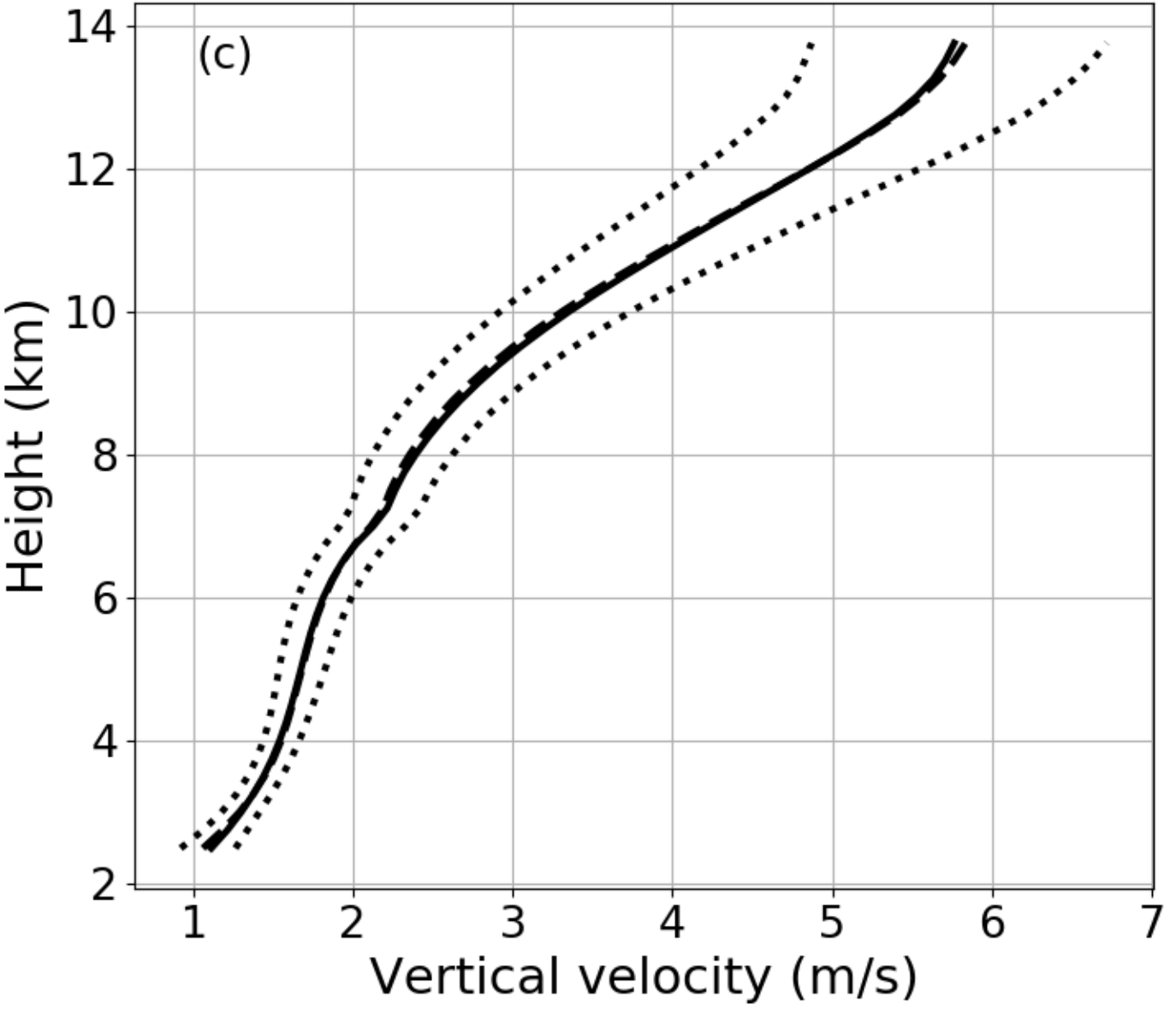
(c)
Height (km)
Vertical velocity (m/s)
14
12
10
8
6
4
2
1
2
3
4
5
6
7

Figure 2d.

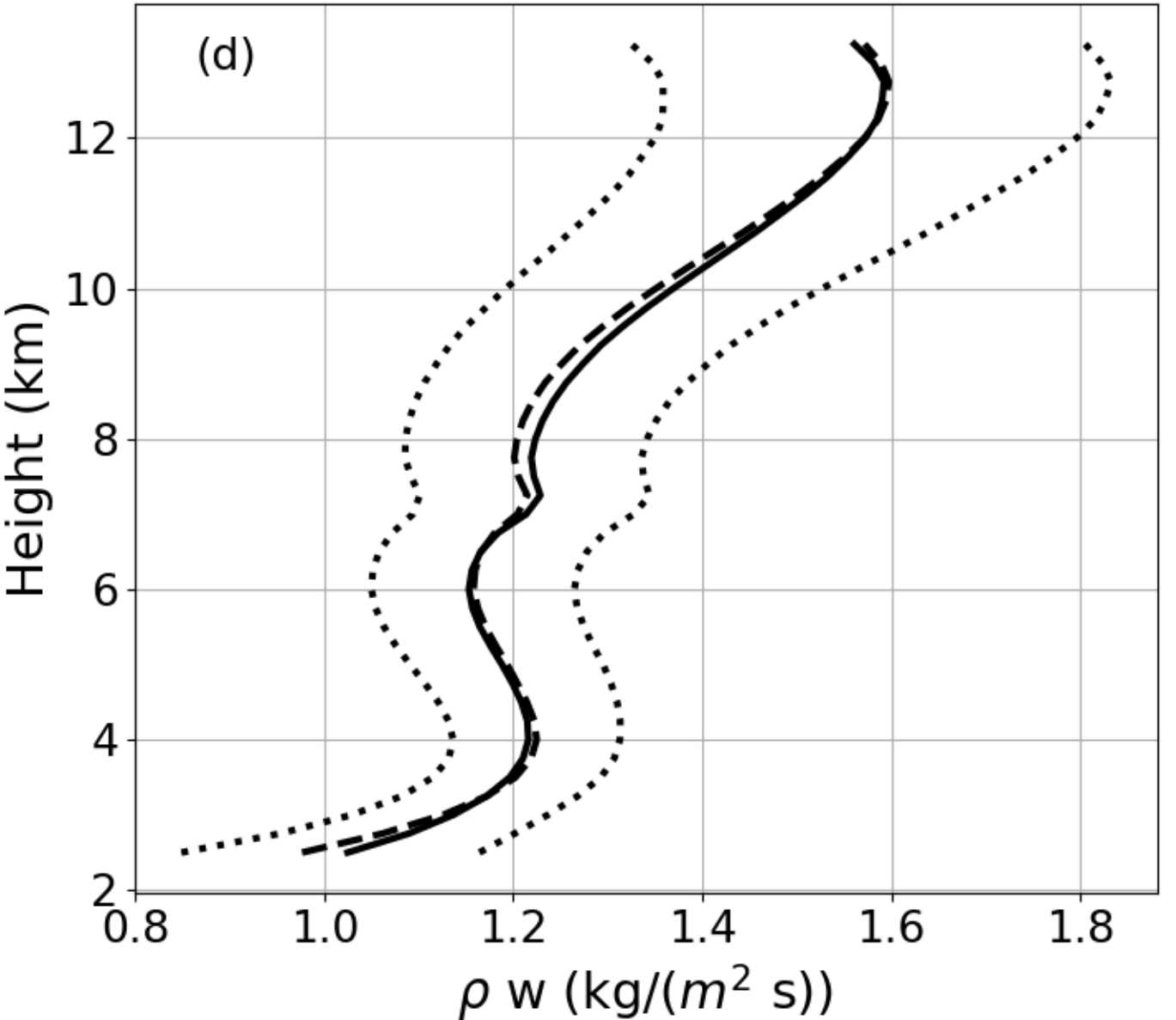
(d)
Height (km)
2
4
6
8
10
12
0.8
1.0
1.2
1.4
1.6
1.8
ρ w (kg/(m² s))

Figure 3a.

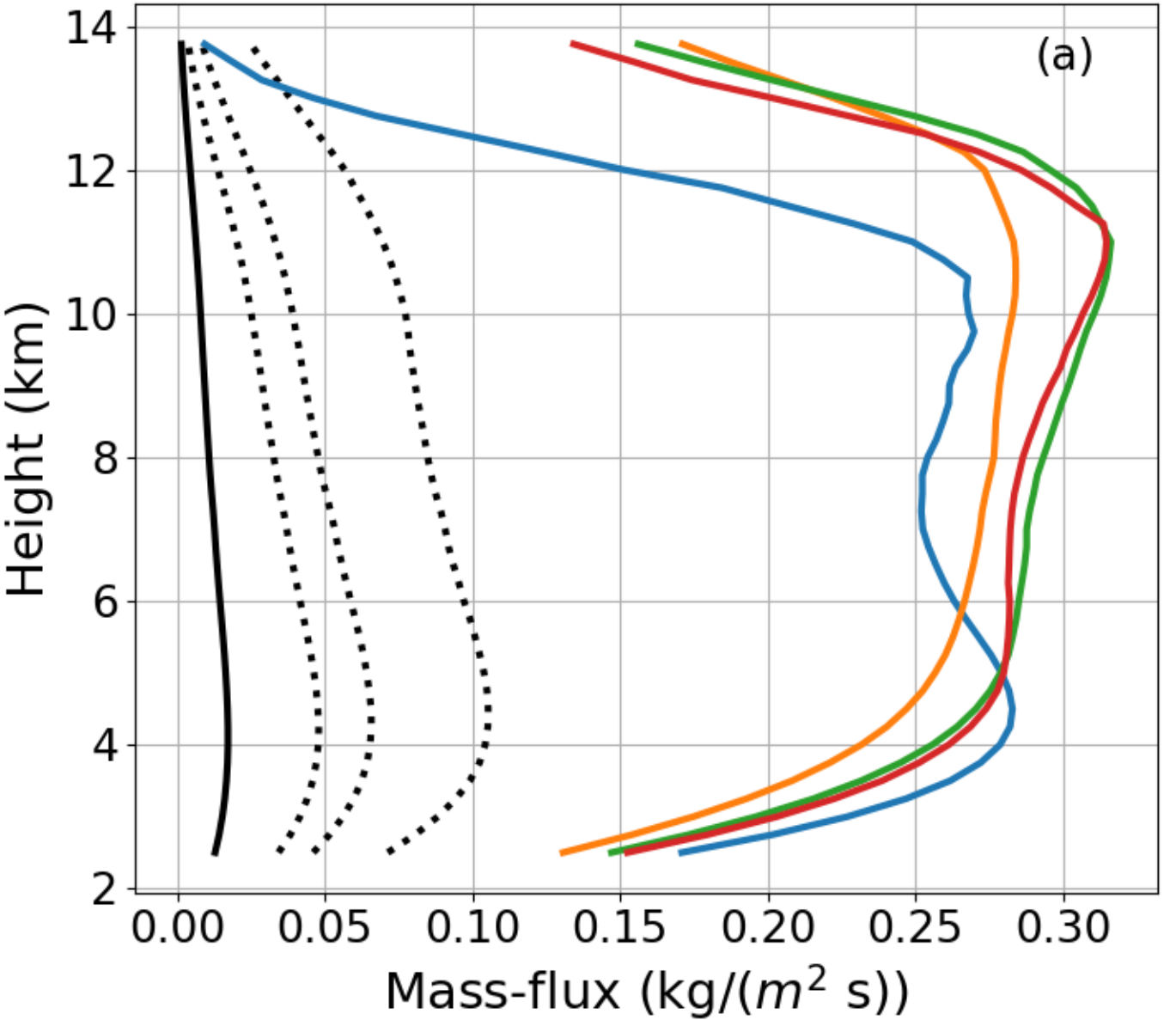
(a)
Height (km)
14
12
10
8
6
4
2
0.00
0.05
0.10
0.15
0.20
0.25
0.30
Mass-flux (kg/(m^2 s))

Figure 3b.

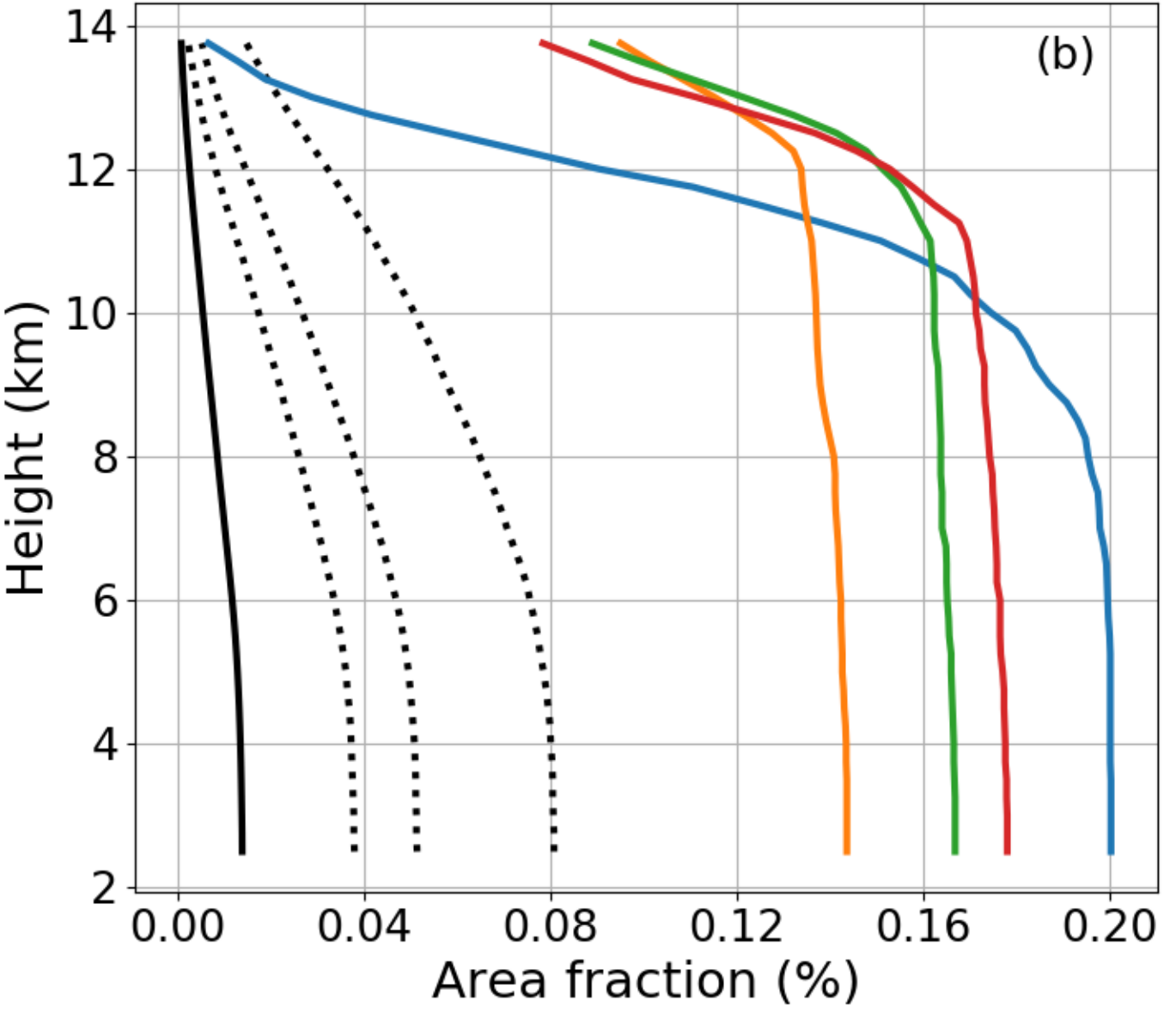
(b)
Height (km)
14
12
10
8
6
4
2
0.00
0.04
0.08
0.12
0.16
0.20
Area fraction (%)

Figure 3c.

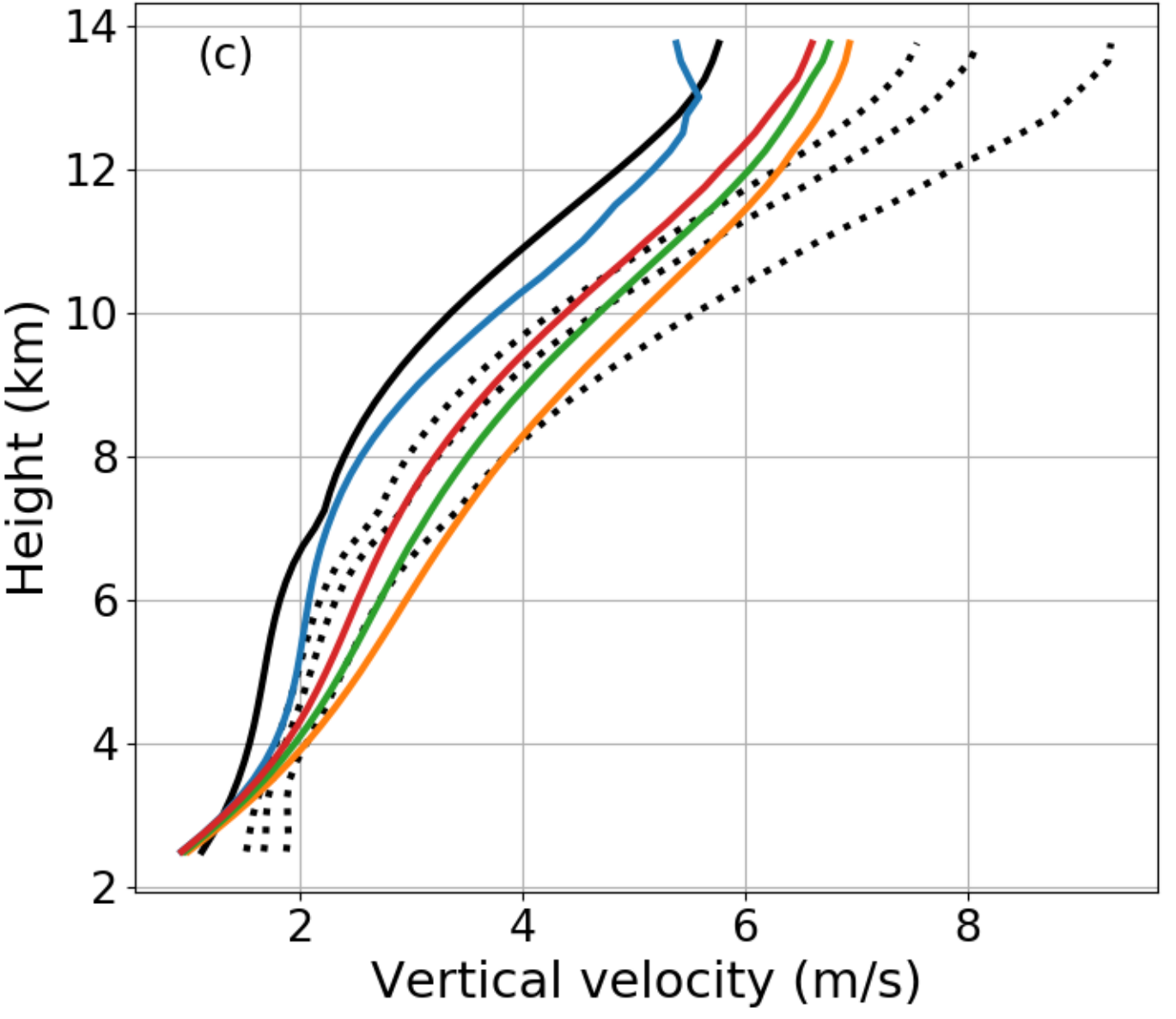
(c)
14
12
10
8
6
4
2
Height (km)
2
4
6
8
Vertical velocity (m/s)

Figure 4a.

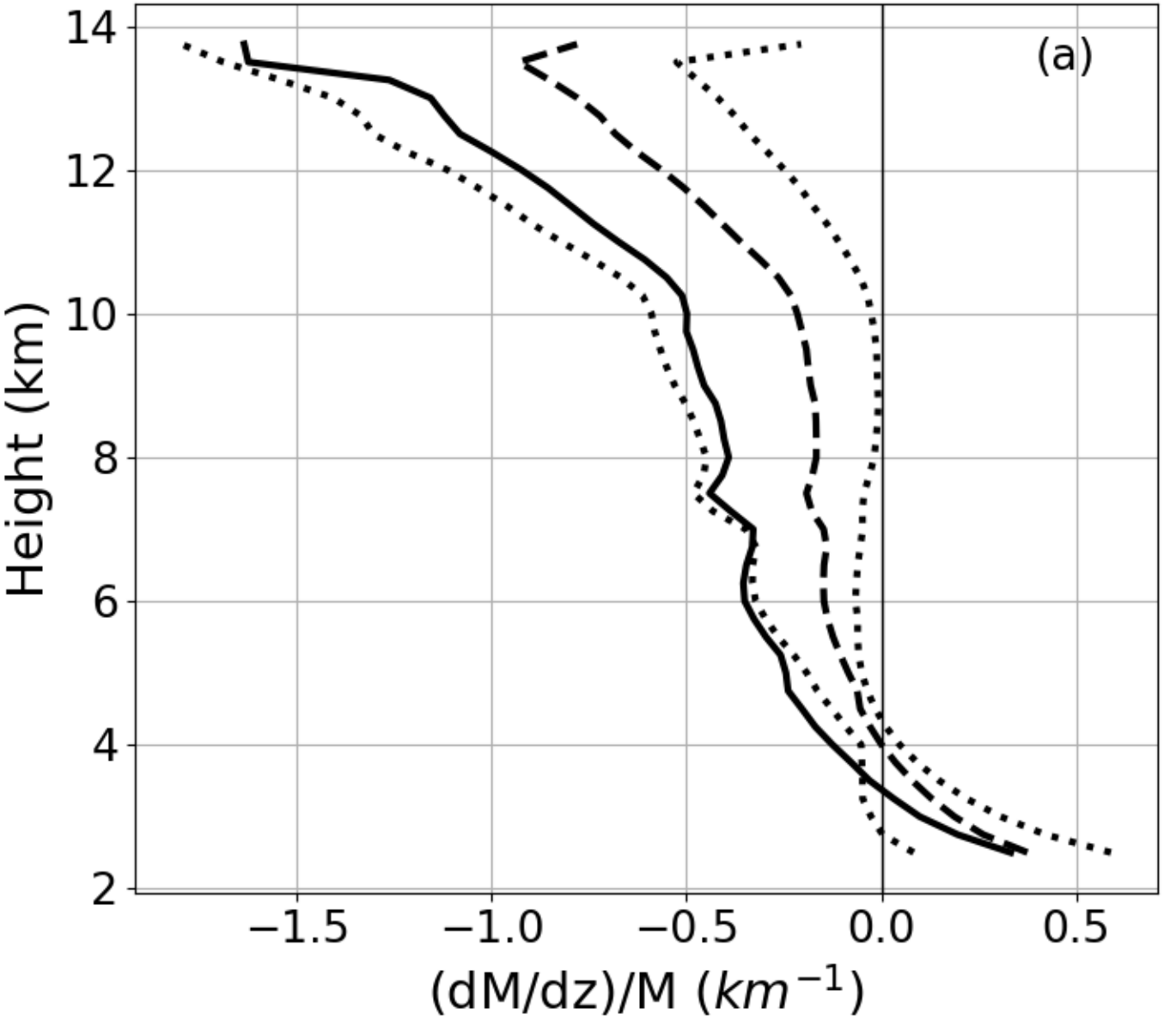
(a)
Height (km)
14
12
10
8
6
4
2
−1.5
−1.0
−0.5
0.0
0.5
(dM/dz)/M (km^{-1})

Figure 4b.

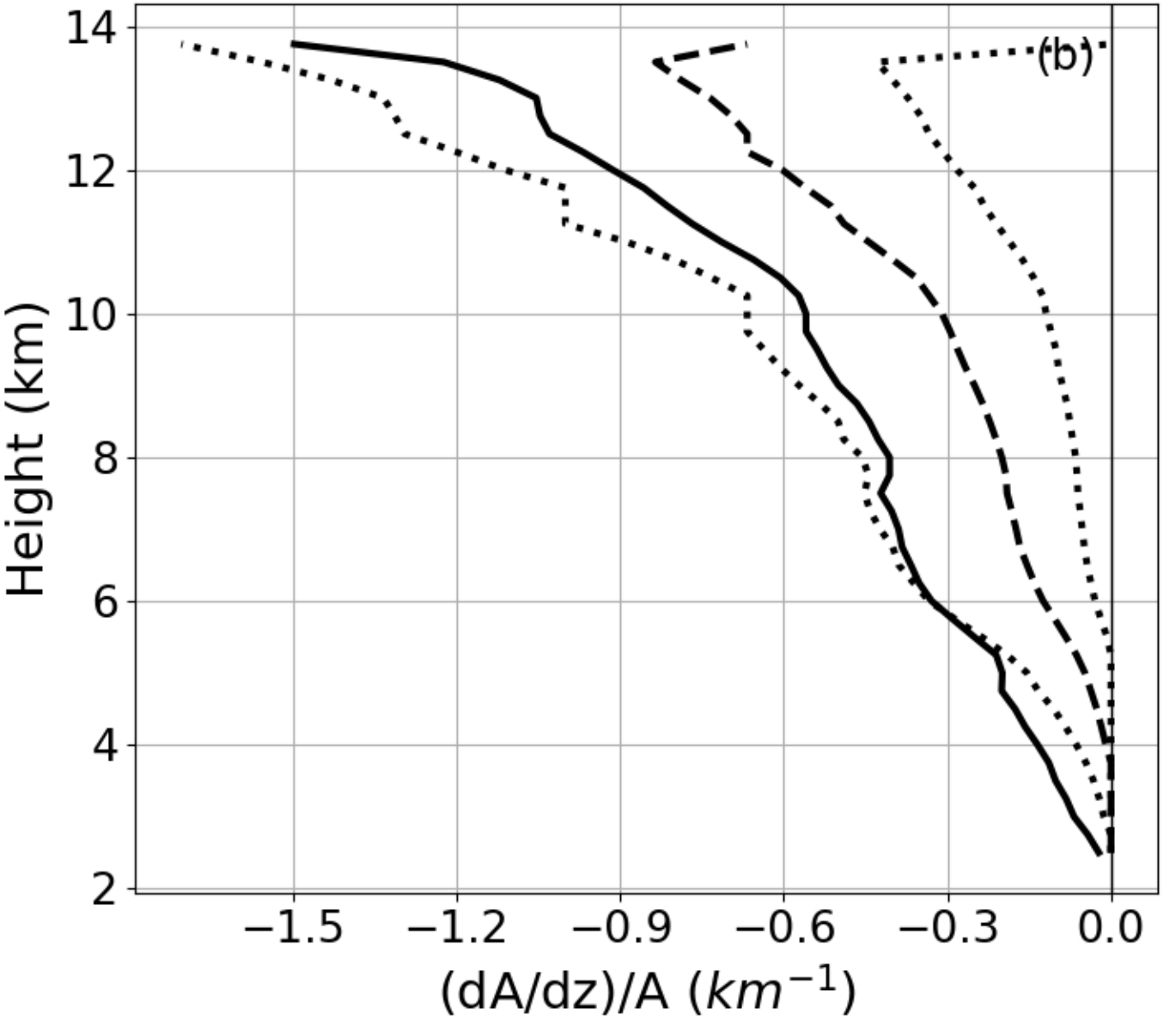
(b)
Height (km)
14
12
10
8
6
4
2
−1.5
−1.2
−0.9
−0.6
−0.3
0.0
(dA/dz)/A (km^{-1})

Figure 4c.

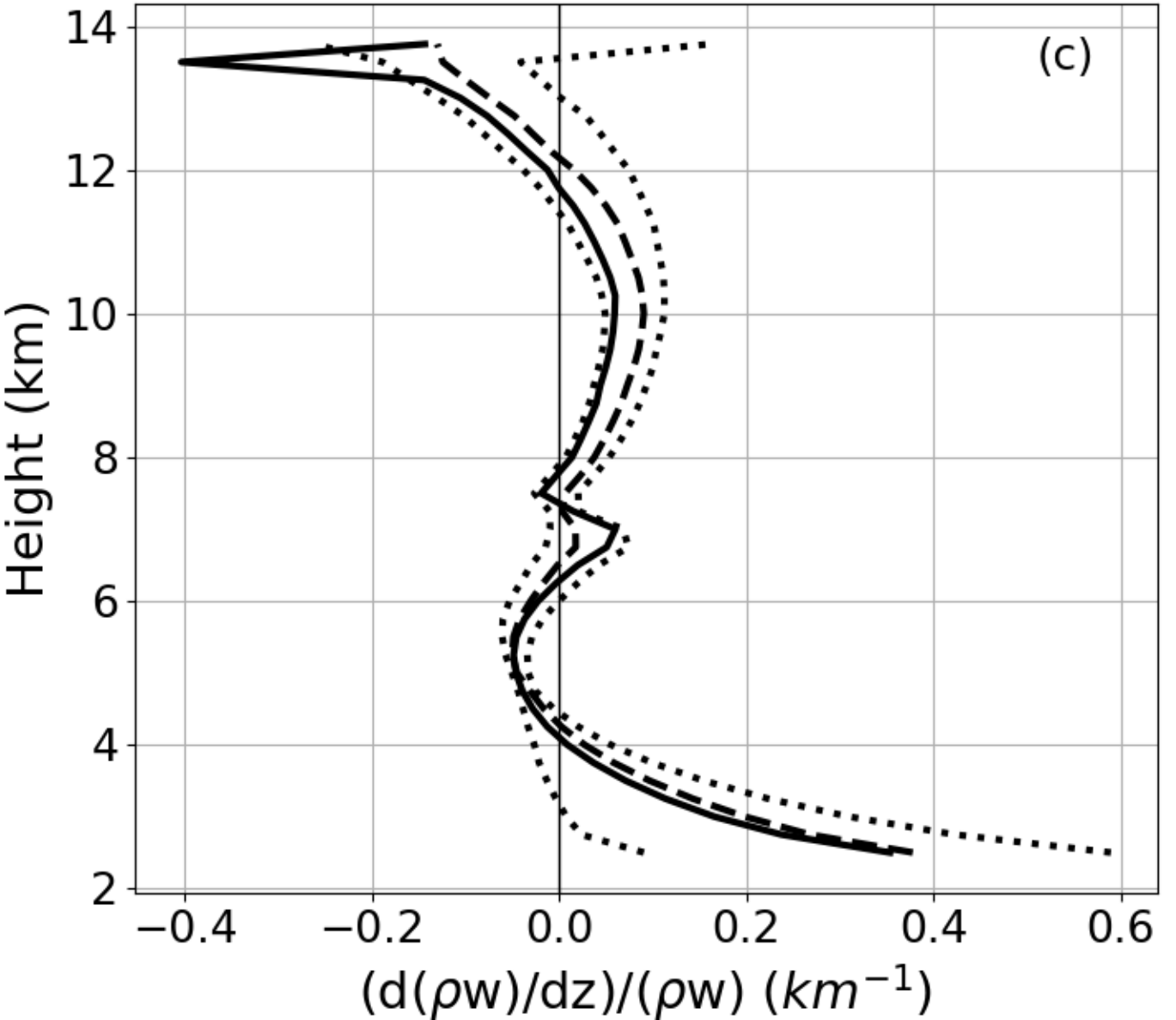
(c)
Height (km)
14
12
10
8
6
4
2
−0.4
−0.2
0.0
0.2
0.4
0.6
(d(ρw)/dz)/(ρw) (km^{-1})

Figure 5a.

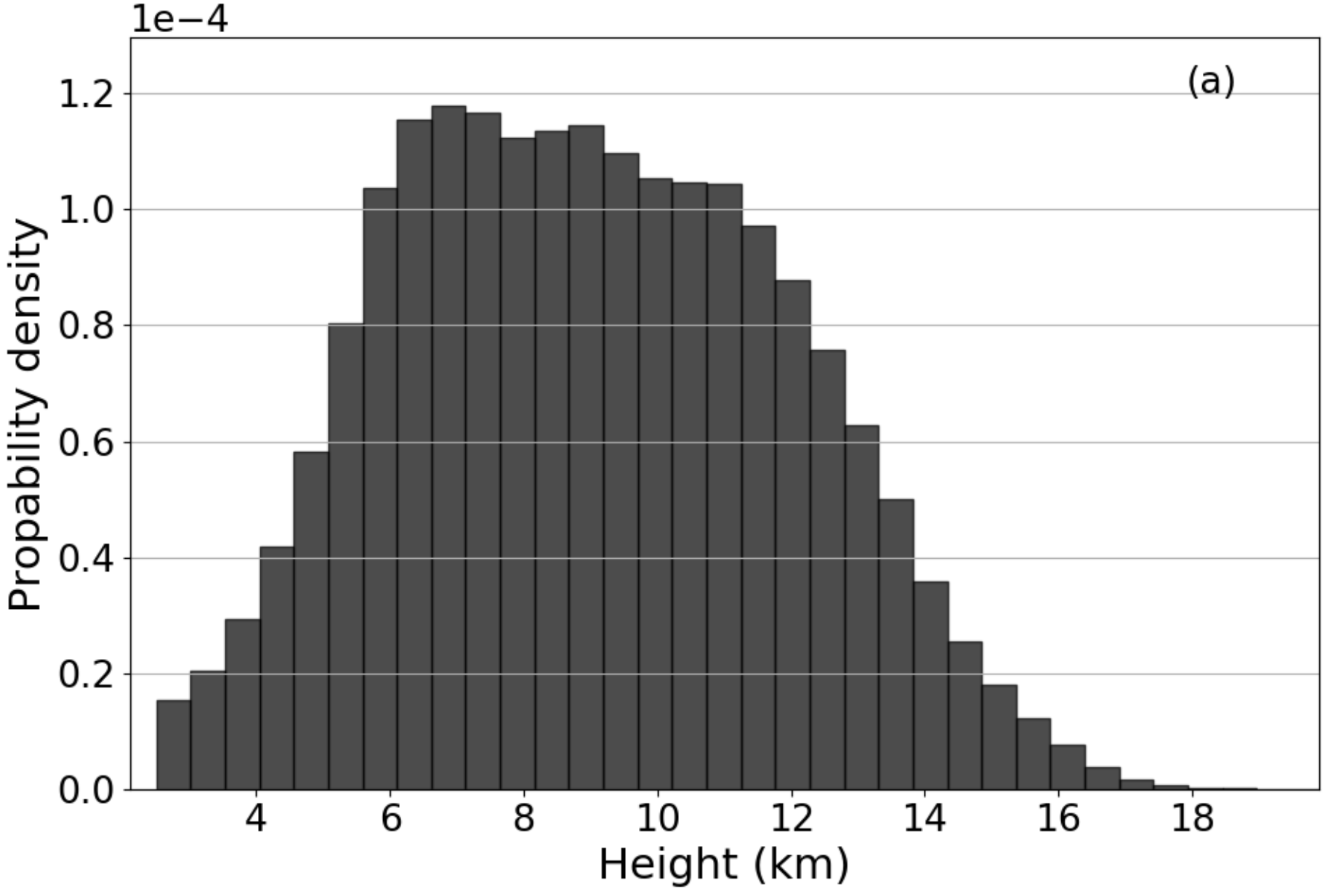
1e−4
(a)
1.2
1.0
0.8
0.6
0.4
0.2
0.0
Propability density
4
6
8
10
12
14
16
18
Height (km)

Figure 5b.

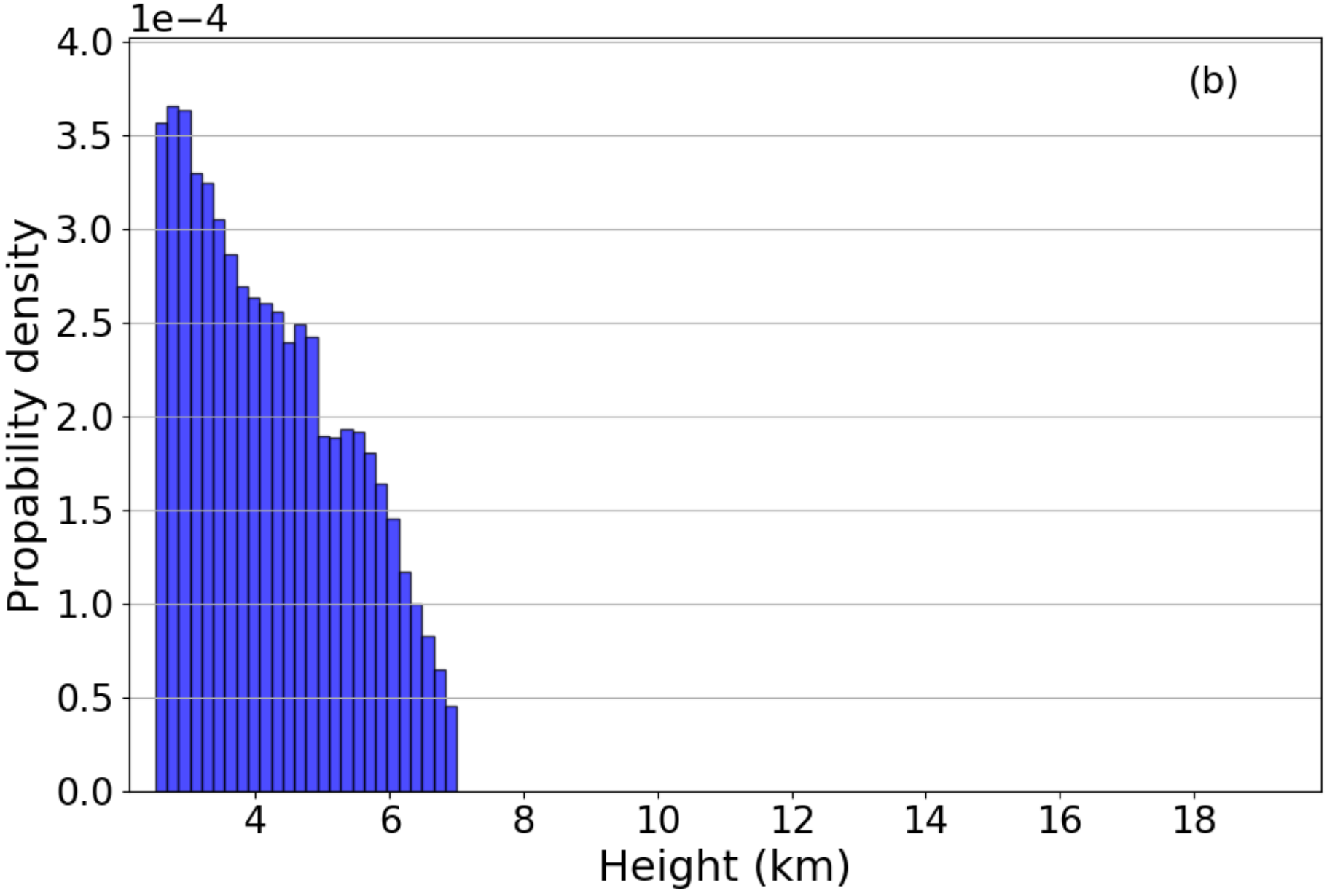
1e−4
4.0
3.5
3.0
2.5
2.0
1.5
1.0
0.5
0.0
Propability density
(b)
4
6
8
10
12
14
16
18
Height (km)

Figure 5c.

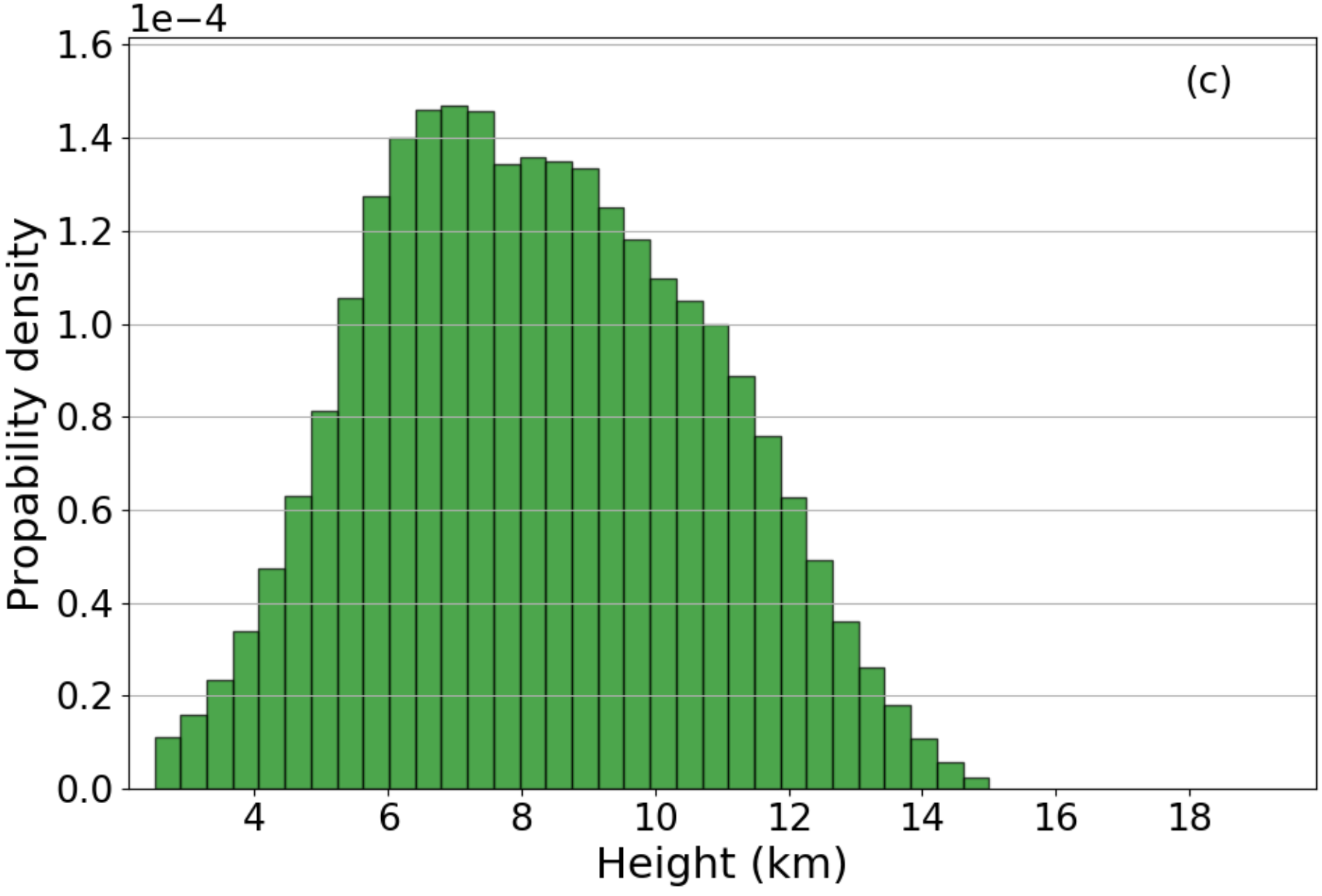
1e−4
1.6
1.4
1.2
1.0
0.8
0.6
0.4
0.2
0.0
Propability density
(c)
4
6
8
10
12
14
16
18
Height (km)

Figure 5d.

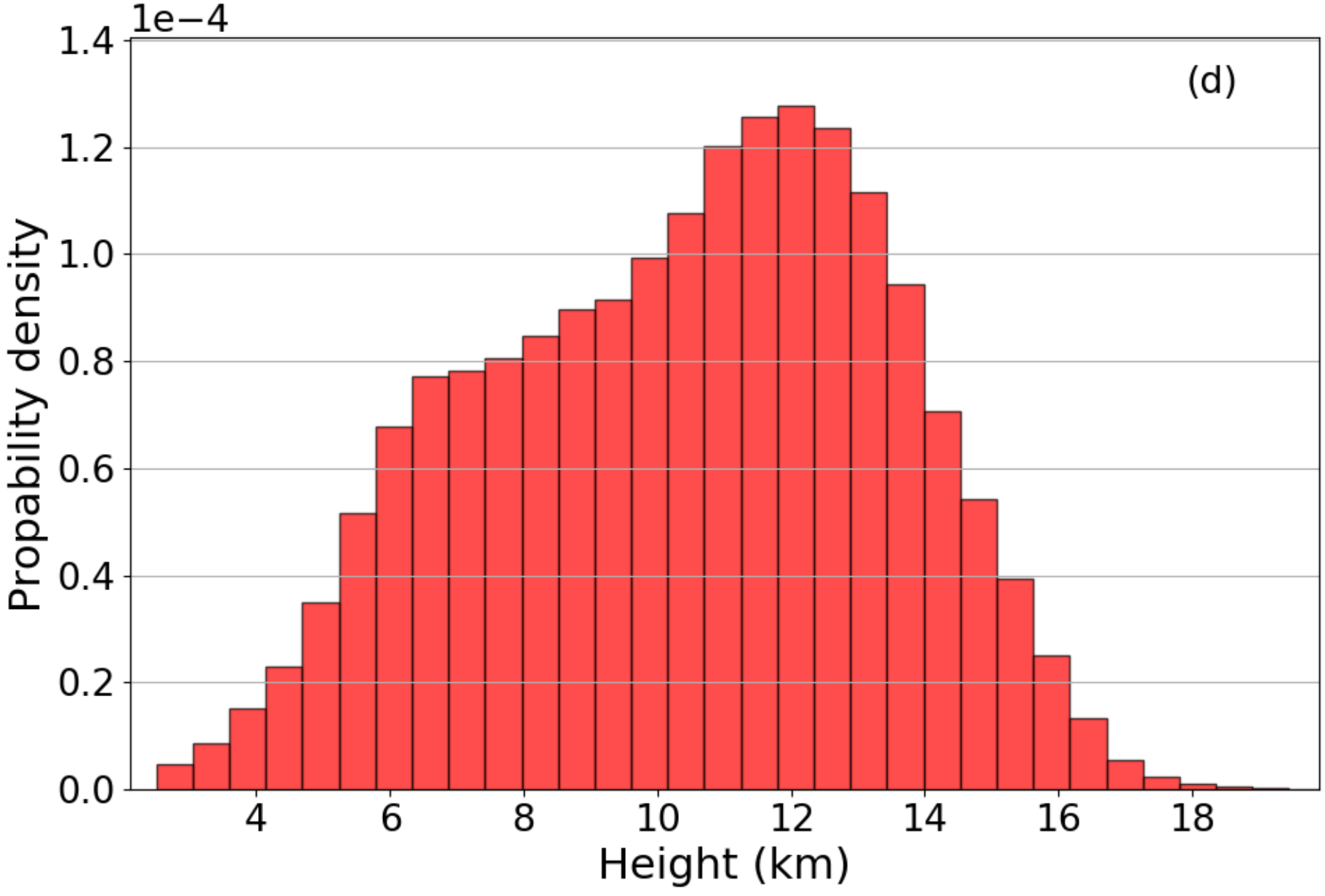
1e−4
1.4
1.2
1.0
0.8
0.6
0.4
0.2
0.0
Propability density
(d)
4
6
8
10
12
14
16
18
Height (km)

Figure 6a.

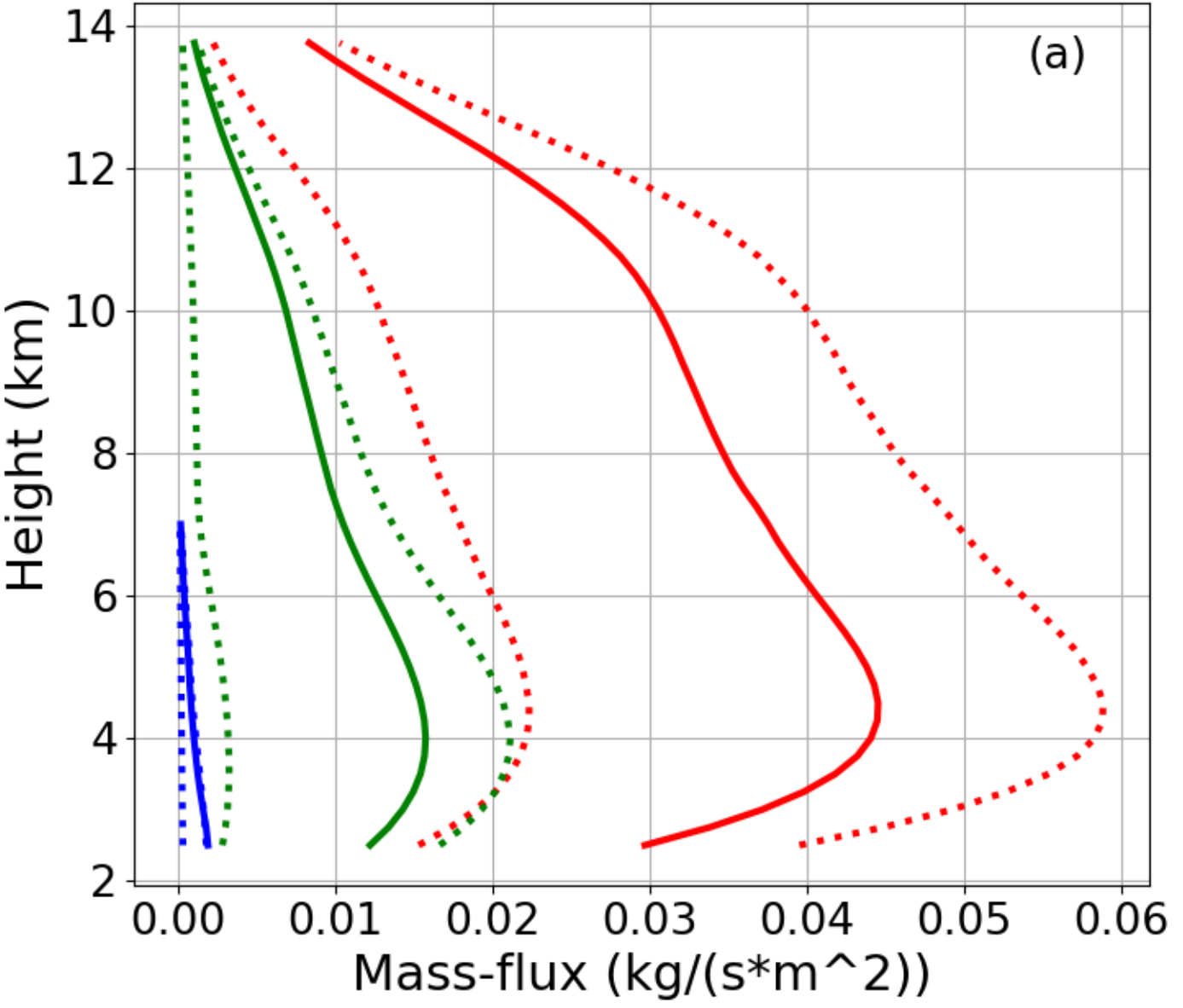
(a)
Height (km)
14
12
10
8
6
4
2
0.00
0.01
0.02
0.03
0.04
0.05
0.06
Mass-flux (kg/(s*m^2))

Figure 6b.

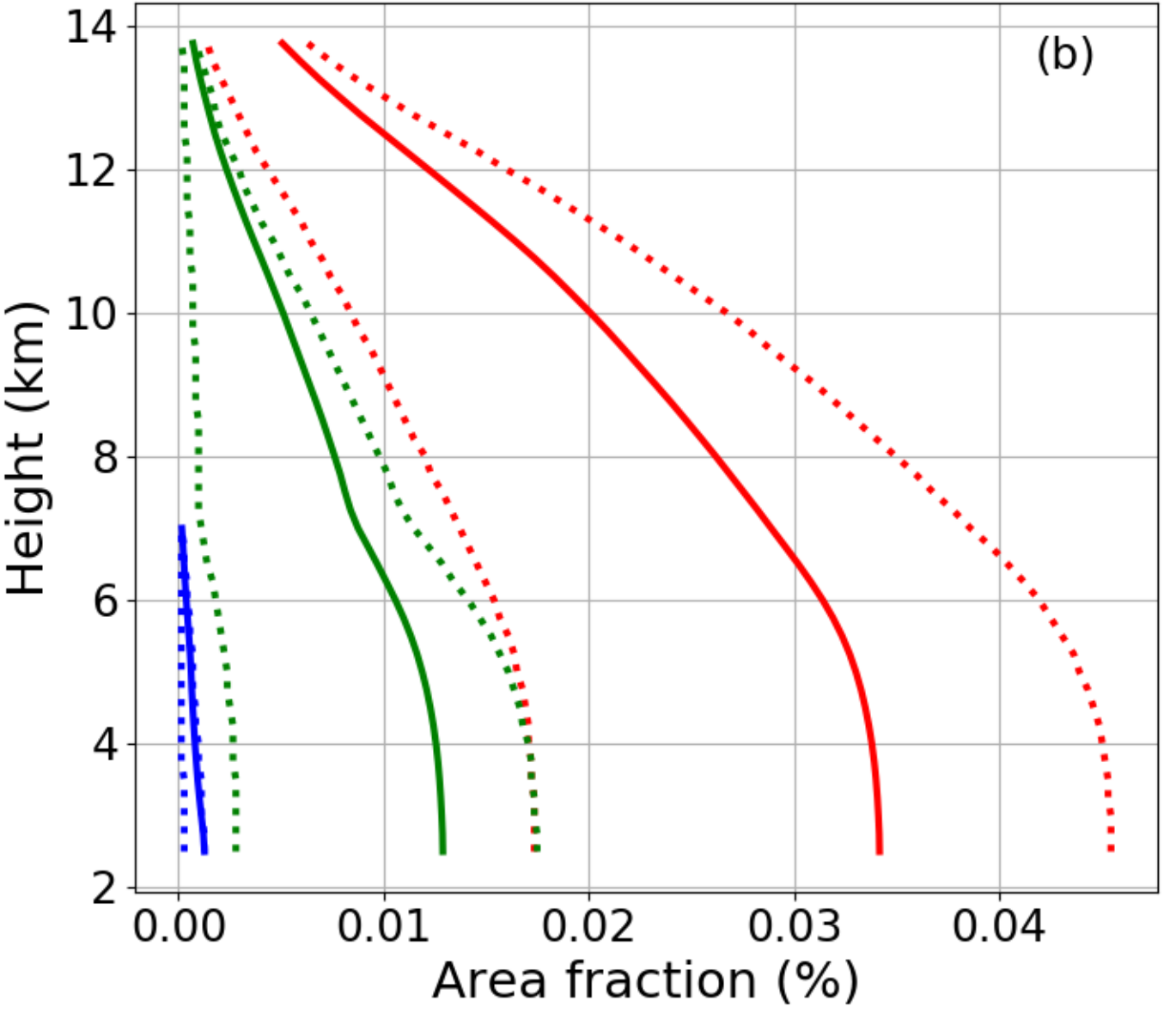
(b)
Height (km)
14
12
10
8
6
4
2
0.00
0.01
0.02
0.03
0.04
Area fraction (%)

Figure 6c.

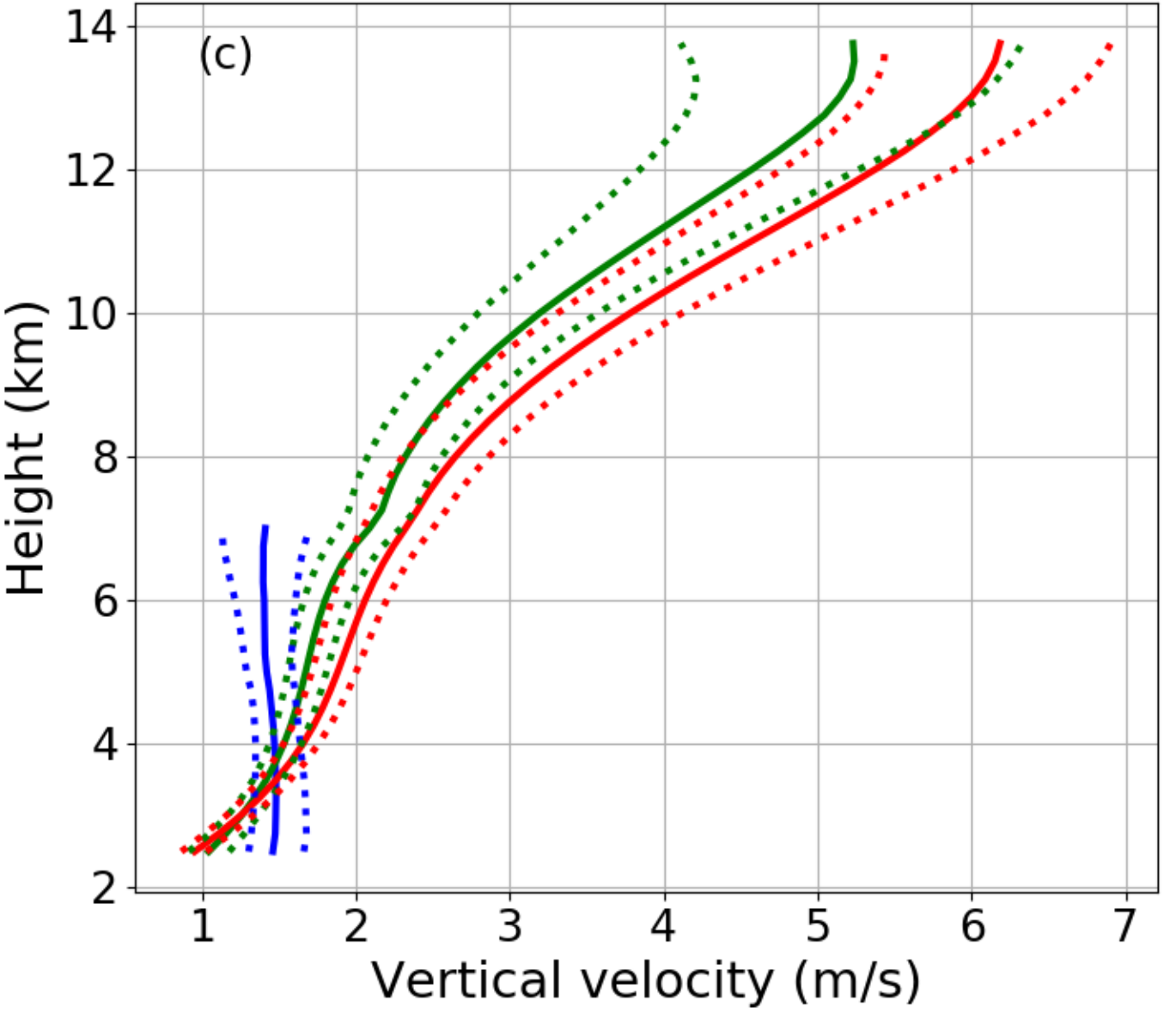
(c)
Height (km)
Vertical velocity (m/s)
14
12
10
8
6
4
2
1
2
3
4
5
6
7

Figure 6d.

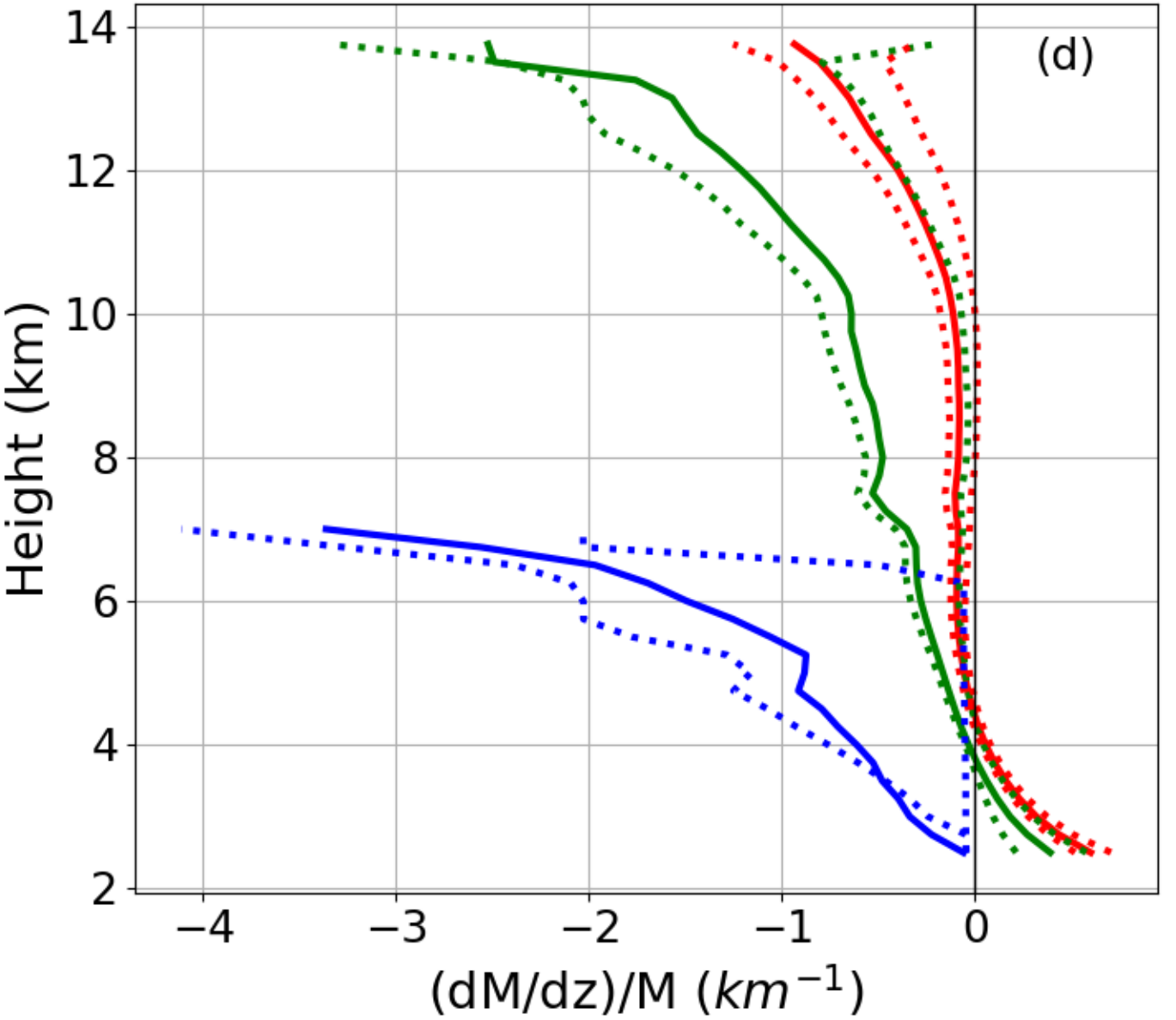
(d)
Height (km)
14
12
10
8
6
4
2
−4
−3
−2
−1
0
(dM/dz)/M (km^{-1})

Figure 6e.

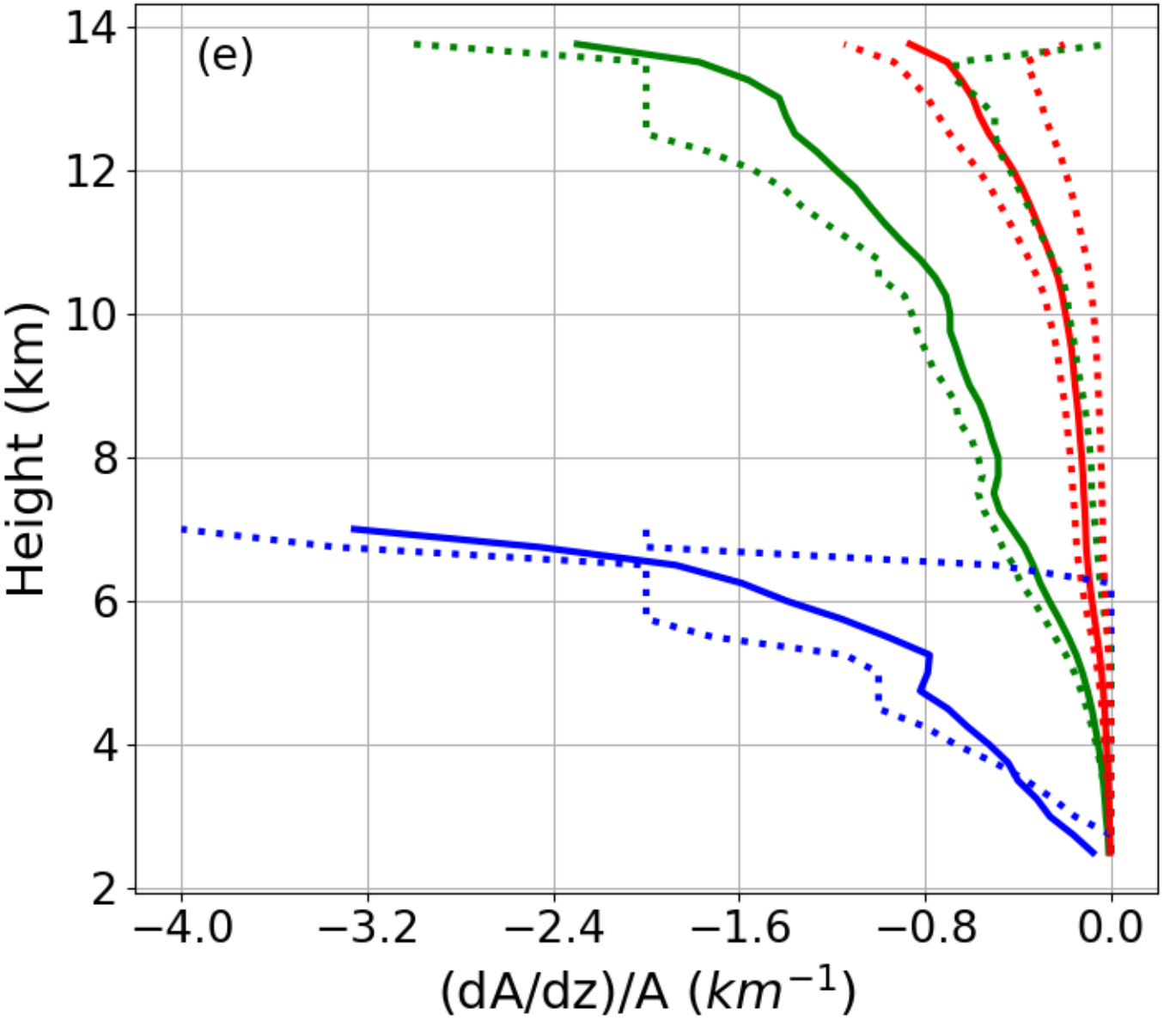
(e)
Height (km)
14
12
10
8
6
4
2
−4.0
−3.2
−2.4
−1.6
−0.8
0.0
(dA/dz)/A (km^{-1})

Figure 6f.

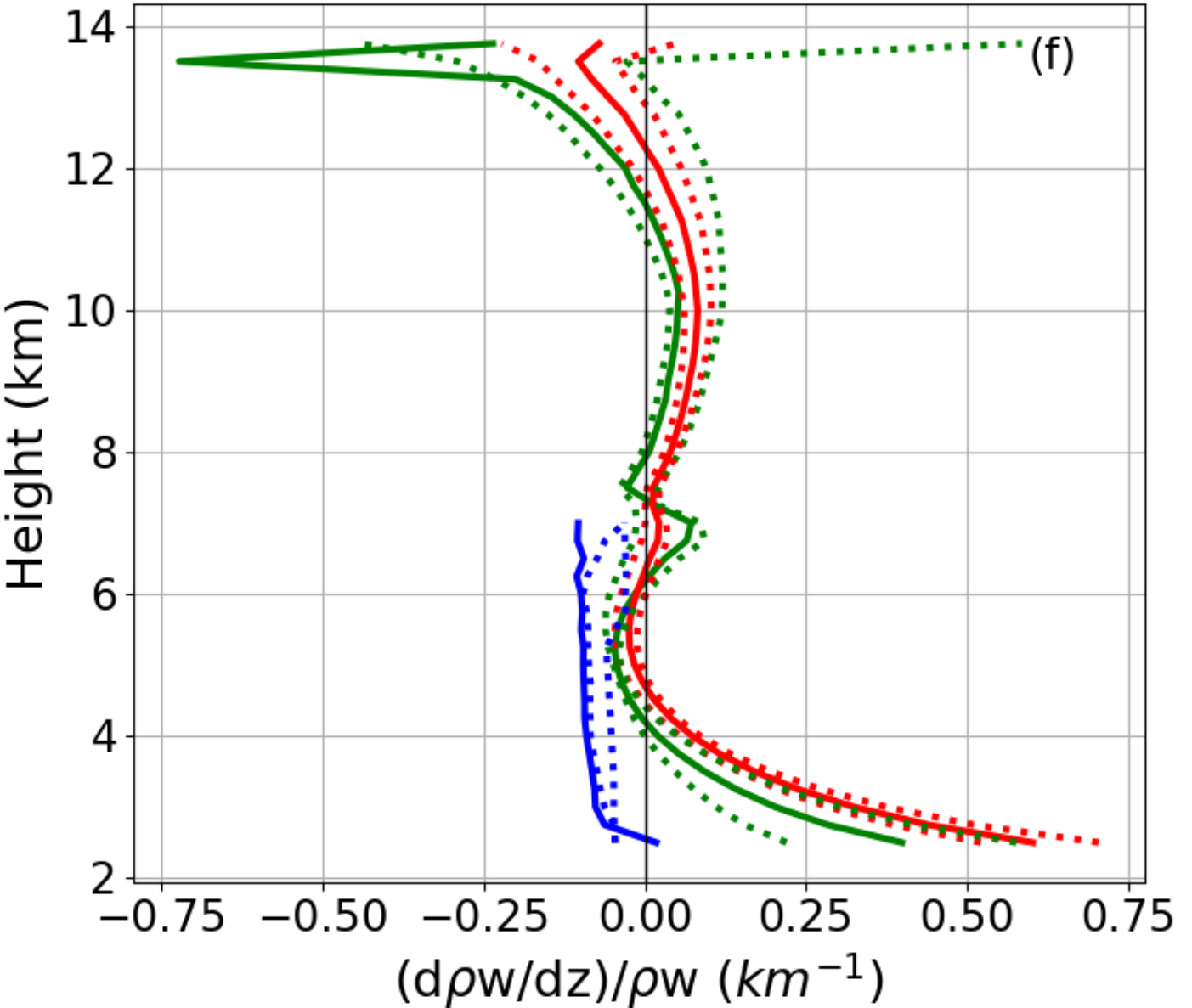
(f)
Height (km)
14
12
10
8
6
4
2
−0.75
−0.50
−0.25
0.00
0.25
0.50
0.75
(dρw/dz)/ρw (km^{-1})

Figure 7a.

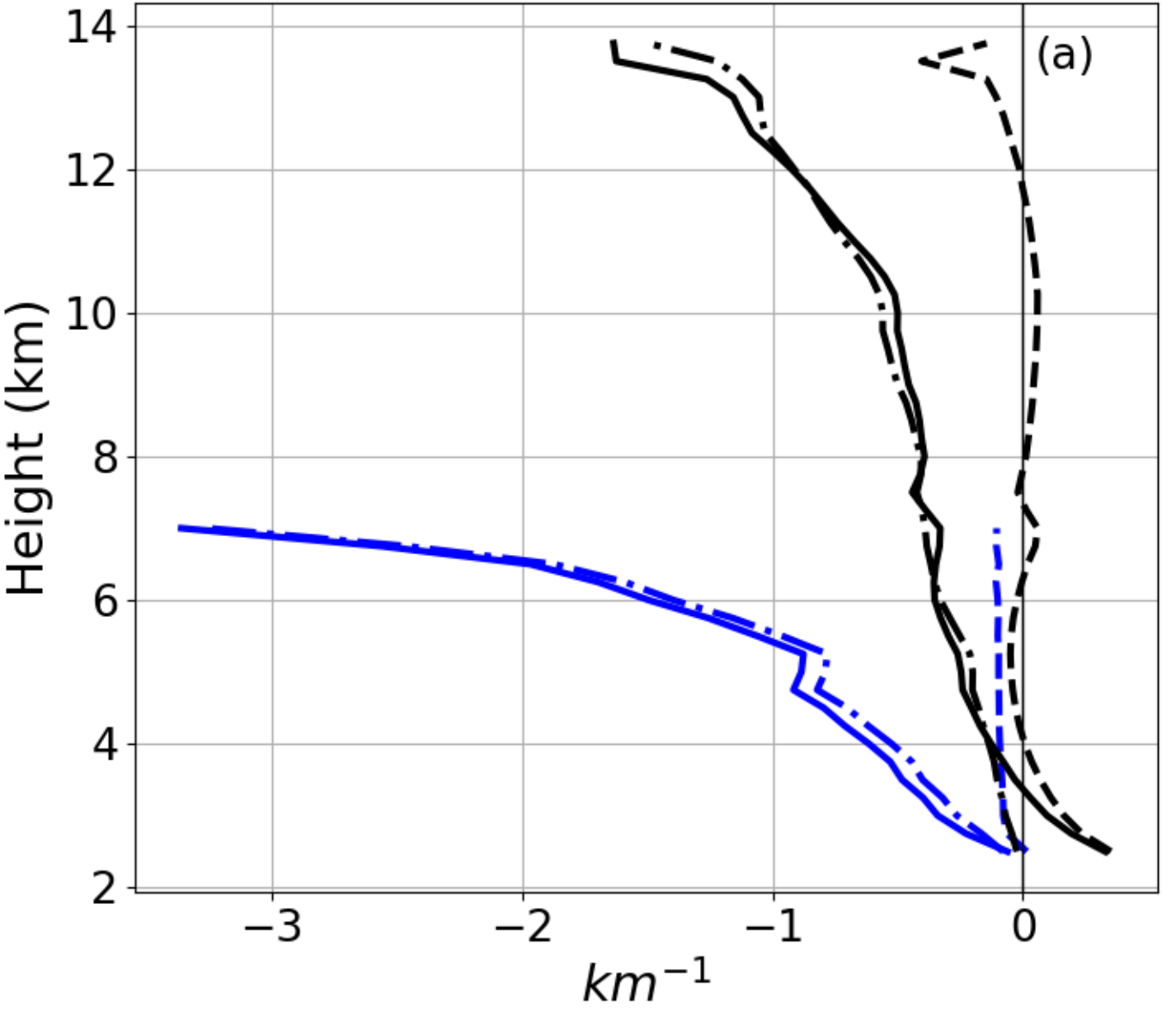
(a)
Height (km)
14
12
10
8
6
4
2
−3
−2
−1
0
km^{-1}

Figure 7b.

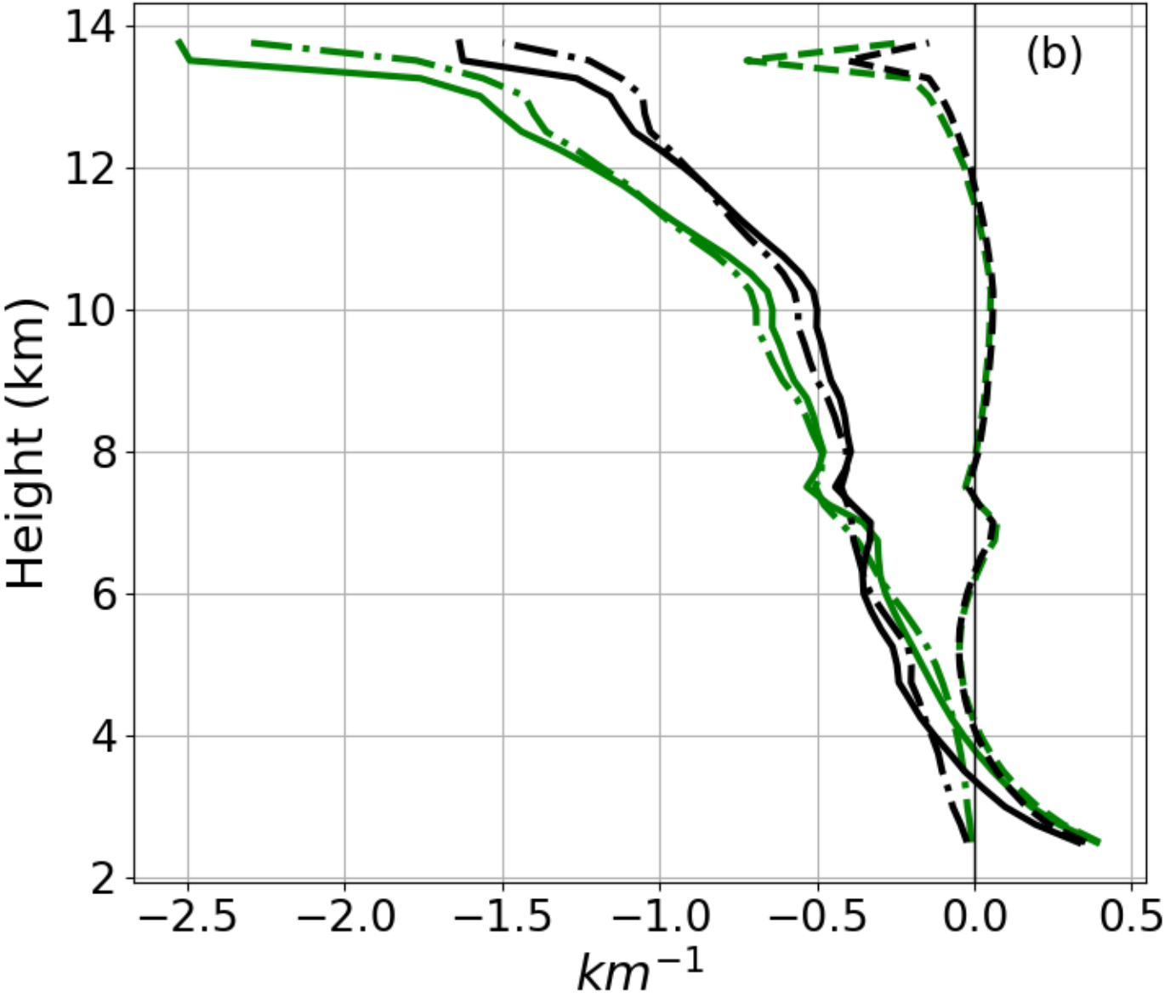
(b)
Height (km)
14
12
10
8
6
4
2
−2.5
−2.0
−1.5
−1.0
−0.5
0.0
0.5
km^{-1}

Figure 7c.

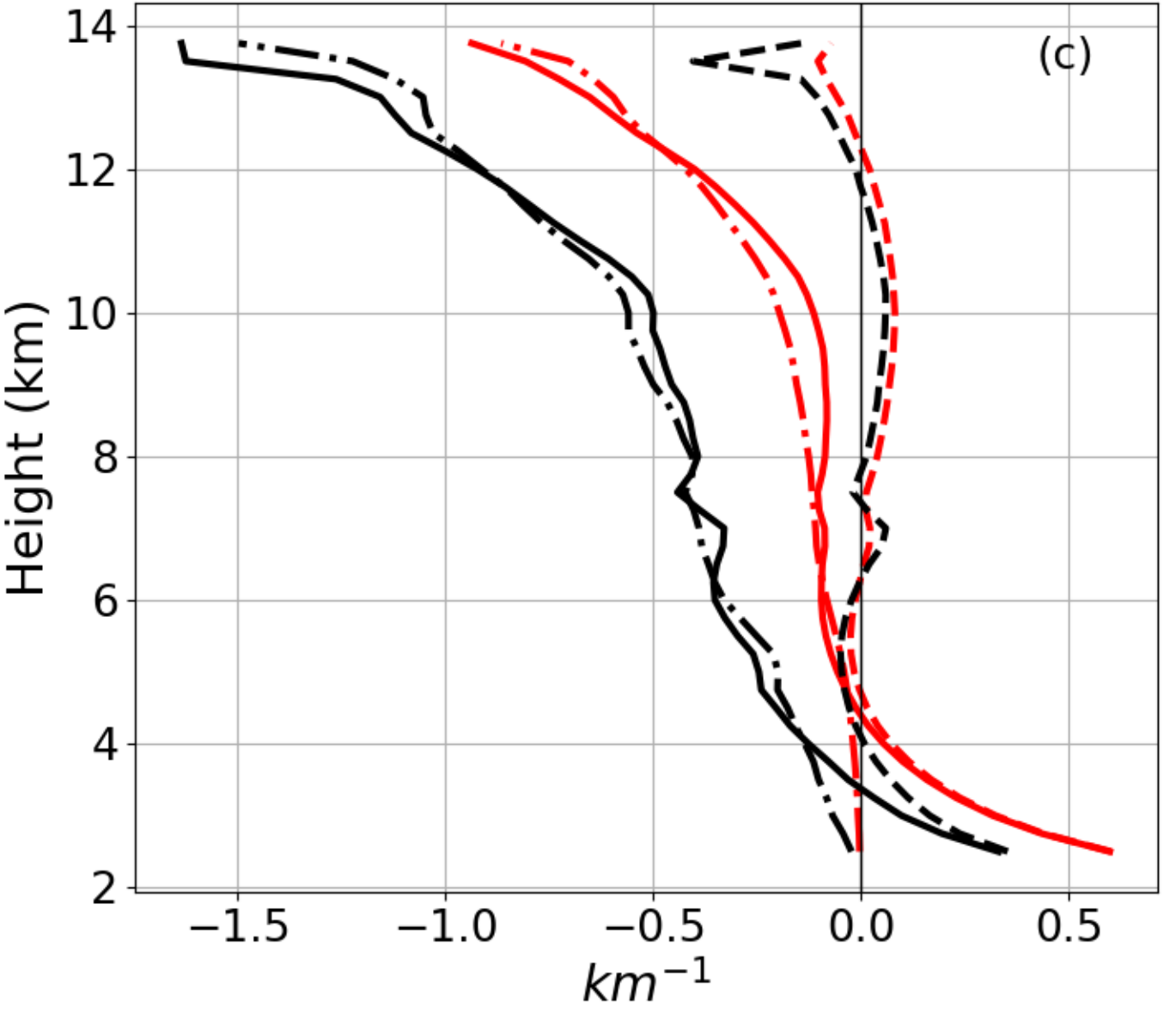
(c)
Height (km)
14
12
10
8
6
4
2
−1.5
−1.0
−0.5
0.0
0.5
km^{-1}